Ore Geology Reviews 163 (2023) 105761

Contents lists available at ScienceDirect

Ore Geology Reviews

journal homepage: www.elsevier.com/locate/oregeorev

Magma and fluid sources in an intracontinental porphyry system: A case study of the Relin Mo–W(–Cu) deposit, southern Yidun terrane, SW China

Fucheng Yang [a,b,c], Rolf L. Romer [b], Johannes Glodny [b], Wenchang Li [a,c,d,*]

[a] School of Earth Sciences and Resources, China University of Geosciences, Beijing 100083, China
[b] Helmholtz Centre Potsdam, GFZ German Research Centre for Geosciences, Telegrafenberg D-14473, Potsdam, Germany
[c] Kunming University of Science and Technology, Kunming 650093, China
[d] Chengdu Center of China Geological Survey, Chengdu 610081, China

A B S T R A C T

The Relin Mo–W (–Cu) deposit in the northern Sanjiang area is bound to a Late Cretaceous intracontinental porphyry showing variable alteration. Here we present whole-rock chemistry and Sr, Nd, Pb, Li, and B isotope data to constrain the sources of ore-magmas and to understand how magmatic-hydrothermal processes mobilize the ore elements and alter the magmatic rocks. Chemical variations indicate the ore-bearing porphyries reflect two processes: fractional crystallization and late-magmatic alteration. Fresh and weakly altered porphyries are metaluminous to weakly peraluminous, showing I-type affinity. Chemical variation among these rocks can be explained by fractional crystallization. Most of these rocks show narrow ranges of isotopic compositions with –8.6 to –6.6 for εNd_{80}, 0.70660 to 0.71028 for $^{87}Sr/^{86}Sr_{80}$, and high $^{207}Pb/^{204}Pb_{80}$ (15.57–15.66) and $^{208}Pb/^{204}Pb_{80}$ (39.21–39.51) values at $^{206}Pb/^{204}Pb_{80}$ values of 17.37 to 18.96. The chemical and isotopic compositions of these rocks indicate that the porphyries represent mantle melts that mixed with partial melts from the Paleoproterozoic crust. Fresh and weakly altered porphyries have uniform δ^7Li (–2.3 to 1.5 ‰) and $\delta^{11}B$ (–8.0 to –12.0 ‰). The strong sericite alteration of the porphyries resulted in the loss of Na_2O and Sr (breakdown of feldspar) and the strong enrichment of the ore elements Cu, Mo, W, and Sn. Porphyries with varying degrees of alteration show large ranges of δ^7Li (–6.0 ‰ to 11.4 ‰) and $\delta^{11}B$ (–8.0 to –29.2 ‰). The anomalously high δ^7Li and low $\delta^{11}B$ values of the altered rocks indicate that the intrusions drove the flow of external fluids that altered the magmatic rocks and leached the ore elements W, Mo, Cu, and Sn from the porphyries and possibly the local wall rocks.

1. Introduction

Porphyry Cu (±Mo) deposits commonly occur in subduction-related continental marginal arc and island arc settings, such as the Andean porphyry Cu belt (Cooke, 2005) or the southwest North American porphyry Cu province (Barra et al., 2005). Porphyry deposits also occur in continental settings, forming collisional and intracontinental porphyry Cu polymetallic deposits, such as the Yulong and Qulong deposits in Tibet (Yang and Cooke, 2019; Wang et al., 2020; Hou et al., 2023). Both subduction-related and continental types of porphyry deposits are spatially and temporally related to porphyry intrusions with the geochemical characteristics of high K-calc-alkaline rocks (Richards, 2003; Hou et al., 2004). Subduction-related magmas were derived from the partial melting of the metasomatized mantle wedge with variable, but generally minor contributions of subducted sediments (Richards, 2011). In contrast, porphyries from continental settings are thought to have formed by the partial melting of juvenile lower crust (Hou et al., 2015; Xu et al., 2021a). Alteration is widely developed around the porphyry intrusions, and the alteration signatures of collisional porphyry deposits are comparable to those porphyry deposits that occur in arc settings (Lowell, 1970). These deposits typically display an inner potassic zone and an outer propylitic zone. These alteration zones were overprinted locally by later phyllic and argillic alteration assemblages (Yang and Cooke, 2019). The primary Cu (± Mo ± Au) mineralization occurs within the potassic and phyllic alteration zones (Yang and Cooke, 2019). Chemical, mineralogical, and isotopic studies reveal that different alteration types may have various fluid sources; early potassic alteration is typically induced by high-temperature magmatic fluid (Seedorff et al., 2005; Ulrich, 2002), whereas the propylitic and phyllic alteration may involve additional contributions of meteoric water to the magmatic fluid (Proffett, 2003; Pacey et al., 2020; Yang et al., 2009). The interaction between the various fluids and the porphyry intrusion resulted in chemical and mineralogical changes in the intrusions and wall rocks (Byrne et al., 2020). These chemical changes involved the addition or removal of some mobile elements (e.g., K, Na, Ca, and Sr) and ore-forming elements (e.g., Cu, Mo, W, and Sn). Hence, understanding the elemental changes and fluid sources during the alteration process is crucial to better understanding the shallow mineralization processes.

The Yidun Cu–Mo–W–Sn–Pb–Zn–Ag polymetallic composite

* Corresponding author at: School of Earth Sciences and Resources, China University of Geosciences, Beijing 100083, China.
E-mail address: lwcyndd@163.com (W. Li).

https://doi.org/10.1016/j.oregeorev.2023.105761
Received 18 June 2023; Received in revised form 10 September 2023; Accepted 30 October 2023
Available online 2 November 2023

metallogenic belt, located in the eastern Tethyan metallogenic domain (Fig. 1A), has metal resources of Cu > 8 million tons (Mt), Mo > 0.6 Mt, W > 0.01 Mt, Sn > 0.1 Mt, and (Pb + Zn) > 0.7 Mt (Zhang, 2018). The huge resource potential makes it an important Cu–Mo polymetallic ore cluster in China. This metallogenic belt experienced a multi–episodic tectonic evolution (Li et al., 2021) and the metallogenic systems associated to granites (porphyries) developed during two major events in the Late Triassic and the Late Cretaceous (Li et al., 2017). These two metallogenic events took place in different tectonic settings: Late Triassic Cu–Pb–Zn mineralization (Fig. 1B, pts. 1–5) formed in a subduction setting (Hou et al., 2007; Li et al., 2011), whereas the Late Cretaceous Mo–Cu–W–Sn–Pb–Zn–Ag mineralization (Fig. 1B, pts. 6–12) is related to an intra-continental extensional setting (Reid et al., 2007; Yang et al., 2020 and references therein).

The Relin porphyry Mo–W (–Cu) deposit, which formed in an intracontinental extensional setting, is a typical example of polymetallic Late Cretaceous mineralization in the southern part of the Yidun metallogenic belt (Fig. 1B). Previous studies indicate an emplacement age of 84–79 Ma for the porphyry intrusions and Re–Os molybdenite ages of 84–81 Ma for the mineralization (Gao et al., 2017; Wang et al., 2014a; Yang et al., 2020). Mineralization stages are characterized by high to medium temperatures (482–268 ℃) and homogeneous $\delta^{34}S$ values (3.5–5.4 ‰) that reflect a magmatic source for sulfur (Gao et al., 2017). These studies demonstrate a close genetic relationship between the porphyry intrusions and the Relin Mo–W (–Cu) mineralization. Several models were proposed for the petrogenesis of the Relin porphyries, including (1) partial melting of the thickened lower crust (Meng, 2014; Wang et al., 2014b) and (2) partial melting of old middle to upper crustal materials (Cao et al., 2016). These controversies on the sources of ore-bearing magmas hinder the understanding of the mechanisms that form porphyry deposits in intracontinental settings. Furthermore, little is known about the behavior of the ore elements (i.e., Cu, Mo, and W) during late-stage magmatic-hydrothermal processes.

In this paper, we focus on the hydrothermal alteration of the Relin porphyries resulting in the mobilization of ore elements and eventually in the formation of Mo–W (–Cu) mineralization. Based on detailed petrographic and geochemical (major and trace elements) analyses, combined with Li–B–Sr–Nd–Pb isotope data, we (1) quantify the chemical changes (gain and loss of elements) during the alteration process; (2) investigate the behavior of the fluid-mobile elements Li and B during alteration of the porphyries related to Mo–W (–Cu) mineralization in an intracontinental setting; and (3) explore the sources of the mineralizing fluids and the economically important metals.

2. Geological setting

2.1. Reginal geology

The Yidun terrane, located at the eastern margin of the Tibetan Plateau, is sandwiched between the Songpan–Ganzi terrane to the east and the Qiangtang terrane to the west (Fig. 1A). The Ganzi–Litang suture and the Jinshajiang suture define the eastern and western boundaries of the Yidun terrane, respectively (Metcalfe, 2021). These two suture zones are considered to include remnants of the Paleo-Tethys oceanic crust (Yin and Harrison, 2000). The western and eastern sections of the Yidun terrane differ in lithology and structure (Reid et al., 2005). The western Yidun terrane, also known as the Zhongza Block (or Zhongza Massif), is a micro-continent fragment that rifted from the Yangtze Block during the Late Permian opening of the Ganzi–Litang Ocean (Reid et al., 2007; Yan et al., 2018). It is composed of Paleozoic marine sedimentary sequences that correspond to the Paleozoic sedimentary units at the western margin of the Yangtze Block (Reid et al., 2005). The eastern Yidun terrane, also known as the Yidun arc (Reid et al., 2007; Li et al., 2017), is the product of the Late Triassic westward subduction of the Ganzi–Litang ocean (Hou et al., 2003; Deng et al., 2014). The eastern Yidun terrane is composed of a Proterozoic basement (i.e., Qiasi Group) and is covered by Paleozoic to Triassic volcanic–sedimentary successions (Tian et al., 2020). These sedimentary rocks were intruded by Triassic (ca. 242 to 203 Ma; Liu et al., 2016) and Cretaceous granitic intrusions (ca. 137 to 75 Ma) (Li et al., 2011a). The emplacement of these granitic intrusions was controlled by the NW- or NNW- trending regional faults, and late-stage NE- and near EW-trending secondary faults (Yu et al., 2020).

No mineralization is known from the western Yidun terrane and only a few Late Triassic granitic intrusions are exposed. In contrast in the eastern Yidun terrane, both Late Triassic and Late Cretaceous granitic intrusions and their wall rocks host major mineralization. Late Triassic mineralization developed in the southern and northern sections of the eastern Yidun belt. In the southern section of the eastern Yidun terrane, mineralization is related to calc-alkaline porphyry intrusions and includes mainly porphyry–skarn Cu deposits, such as the Pulang (Cu: 5.11 Mt @ 0.52%), Xuejiping (Cu: 0.29 Mt @ 0.53%), Lannitang (Cu: 0.18 Mt @ 0.5%), and Chundu (Cu: 0.15 Mt @ 0.51%) deposits (Fig. 1B; Li et al., 2022; Yang and Cooke, 2019). In the northern section of the eastern Yidun terrane, mineralization is bound to intra-arc rift basins with bimodal volcanic rocks (rhyolite and basalt) and associated volcanogenic massive sulfide (VMS-type) Cu–Pb–Zn deposits (e.g., Gacun, Cu + Pb + Zn: 4 Mt; Hou et al., 2007). The Late Cretaceous mineralization mainly includes porphyry–skarn–hydrothermal vein Mo–W–Cu–Sn–Pb–Zn–Ag deposits related to granite (porphyry) intrusions that occur along the entire belt (Fig. 1B). Major deposits include the Xiuwacu and Relin porphyry–hydrothermal Mo–W (–Cu) deposits, Hongshan, Tongchanggou, and Donglufang porphyry–skarn Mo–Cu deposits in the south (Zhang et al., 2021) and the Xiasai vein-type Ag–Pb–Zn (–Sn) deposit and Cuomolong skarn Sn deposit in the north (Yang et al., 2020).

2.2. Deposit geology

The Relin Mo–W (–Cu) deposit is located in the southern section of the Yidun terrane (Fig. 1B). Triassic diorite porphyries and Late Cretaceous granites are exposed in the Relin deposit. The Late Cretaceous granites intrude Late Triassic sedimentary rocks of the Qugasi and Tumugou formations (Fig. 2). The Qugasi Formation is composed of slate, metasandstone, and limestone, whereas the Tumugou Formation consists of slate and intermediate-acid volcanic rocks with interbedded limestone. The Mo–W (–Cu) mineralization at Relin is hosted by the Late Cretaceous monzogranite porphyry (83–77 Ma) whose emplacement was controlled by NW-trending faults (Wang et al., 2014a; Gao et al., 2018). The porphyries and their hornfel wall rocks host disseminated and vein (quartz + pyrite + molybdenite + chalcopyrite ± scheelite) mineralization. Hydrothermal alteration associated with Mo–W (–Cu) mineralization is dominated by sericitic alteration and minor potassic alteration. There are four NW-trending main orebodies, 50–200 m long and 0.6–3.0 m wide with grades of 0.031 % to 0.23 % Mo and 0.071 % to 0.21 % WO_3 (Dong et al., 2022). Ore minerals are molybdenite, chalcopyrite, and scheelite.

2.3. Sample descriptions

Fourteen porphyry and four wall rock samples are collected from drill holes and surface exposures in the mining area. Based on different degrees of high-temperature alteration and mineralization, the porphyries were distinguished into three types, i.e., Type I is not mineralized and fresh (Fig. 3A); Type II has Mo–W (–Cu) mineralization (Fig. 3B–D); and Type III has W (–Mo) mineralization (Fig. 3E and Fig. 4A). Type I porphyry is grey, has a porphyritic texture (Fig. 3G), and is composed of plagioclase (35 vol%), K-feldspar (30 vol%), quartz (20 vol%), biotite (10 vol%), and amphibole (5%). Type II porphyry, which is closely associated with Mo–W (–Cu) mineralization, includes three sub-types, i.e., II-1, II-2, and II-3 that differ in color and intensity of alteration. Type II-1 is weakly sericitized grey porphyry with plagioclase

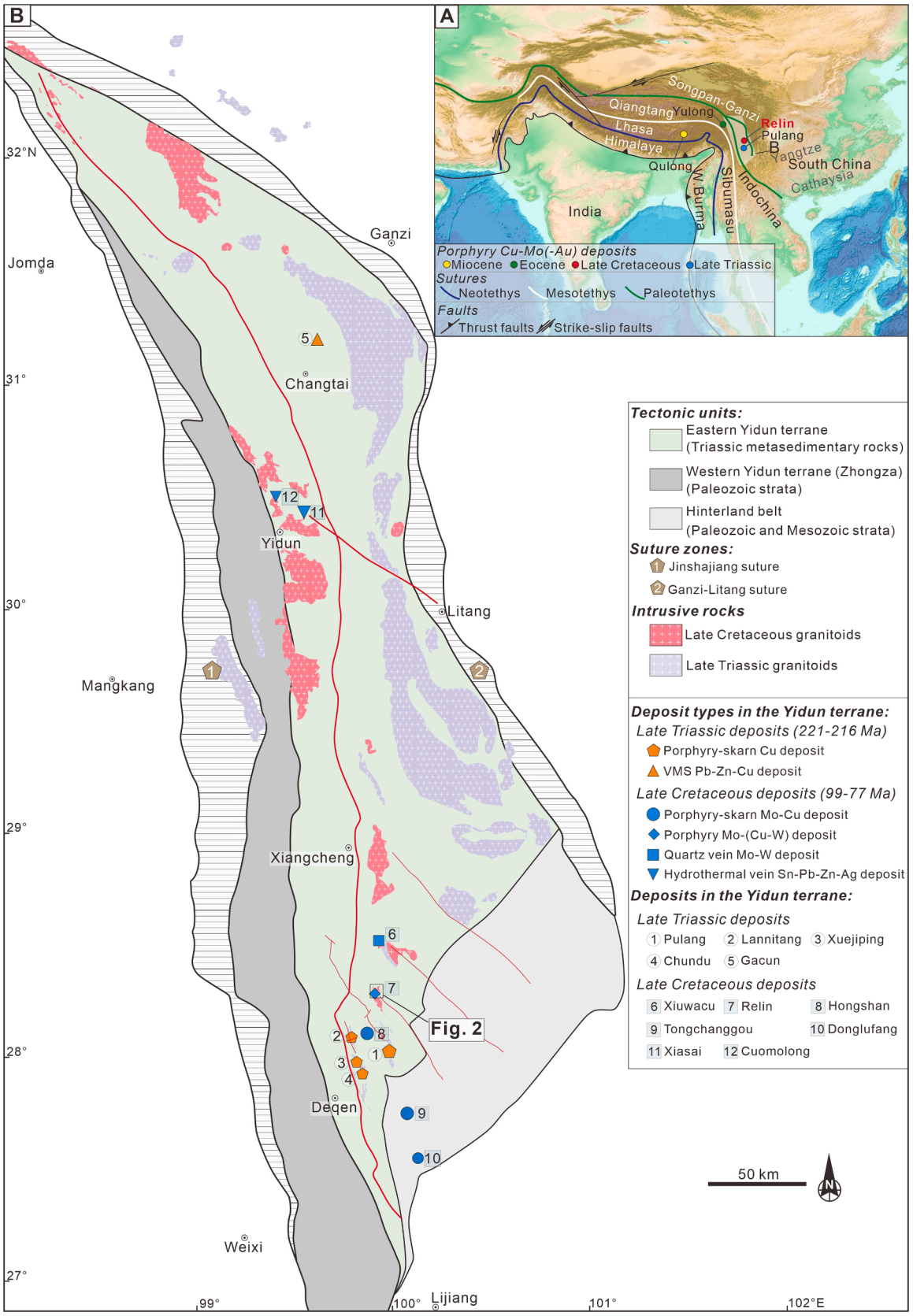

Fig. 1. (A) Topographic map showing the distribution of major sutures and tectonic blocks in the eastern Tethyan metallogenic domain and the location of the study area (modified after Richards, 2015). (B) Simplified geological map of the Yidun terrane, showing the distribution of Late Triassic and Late Cretaceous granitic intrusions and associated deposits of Mo, Cu, W, Sn, Pb, Zn, and Ag (modified after Li et al., 2017; Jackson et al., 2020).

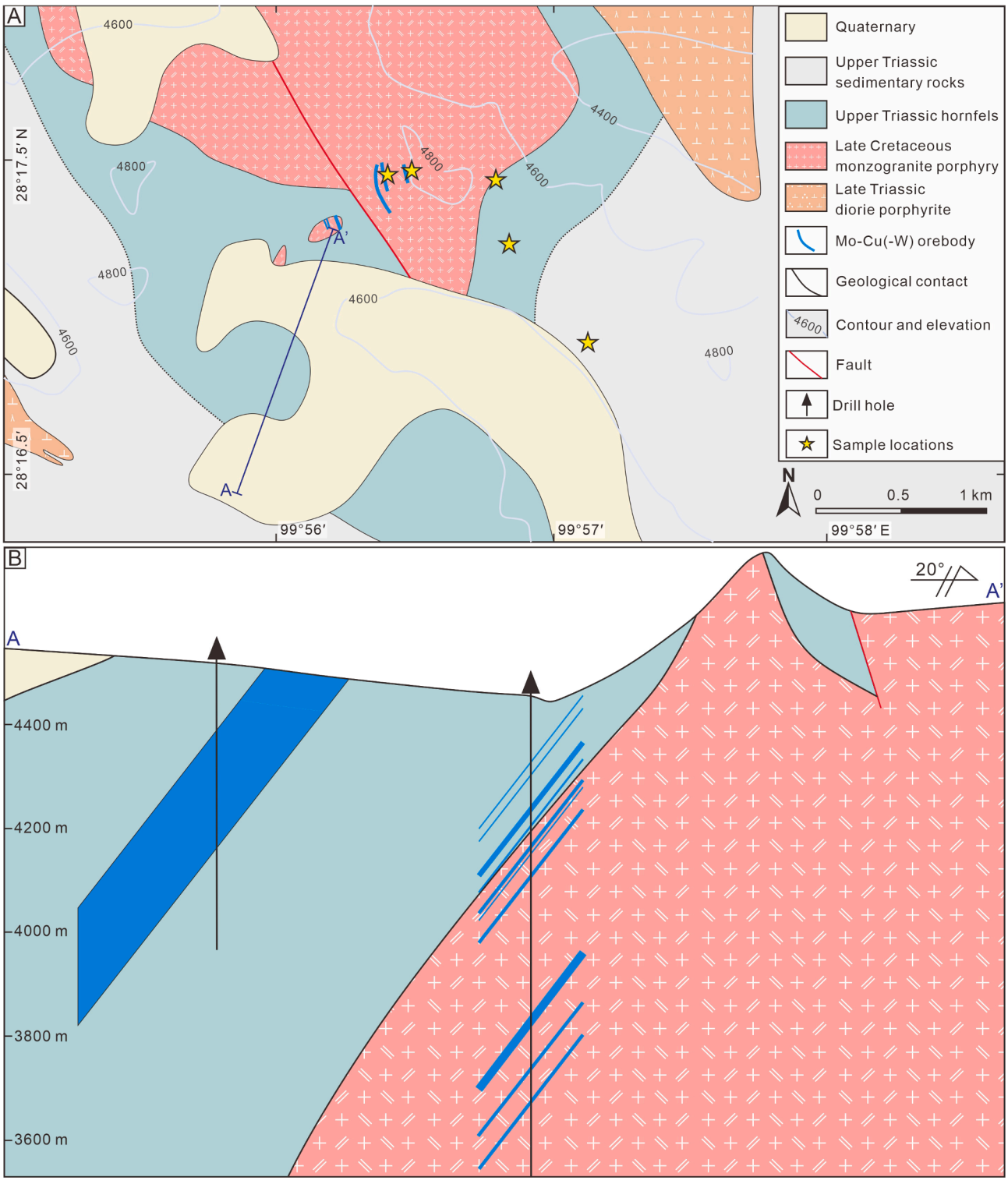

Fig. 2. (A) Simplified geological map showing the location of the Relin deposit and the distribution of associated Late Cretaceous intrusions and Triassic wall rocks; (B) Cross-section (A-A') map showing the relation between the porphyry and ore bodies.

and biotite locally showing weak alteration to sericite (Fig. 3H). Type II-2 is moderately sericitized porphyry, is yellow to green, and plagioclase and biotite are largely replaced by sericite. Type II-3 is strongly sericitized porphyry that is yellow to green due to the nearly complete alteration of plagioclase and biotite to sericite (Fig. 3I). Type III porphyry has vein-type W (–Mo) mineralization (quartz + scheelite ± molybdenite) and includes two subtypes. Type III-1 is weakly sericitized porphyry with plagioclase being selectively altered to sericite and quartz–scheelite veinlets (Fig. 4A). Type III-2 is a strongly altered porphyry that shows quartz–scheelite stockwork with the plagioclase near the veins being completely altered to sericite (Fig. 3E).

Four porphyry samples (i.e., P-I, P-II, P-III, and P-IV) with variable degrees of alteration toward mineralized veins were cut along profiles into slices of contrasting alteration. Profile P-I (sample 15RL5-6; Fig. 4A) includes five slices with increasing alteration from P-I-1 (weakly altered) to P-I-4 (moderately altered). P-I-5 is dominated by the alteration halo of

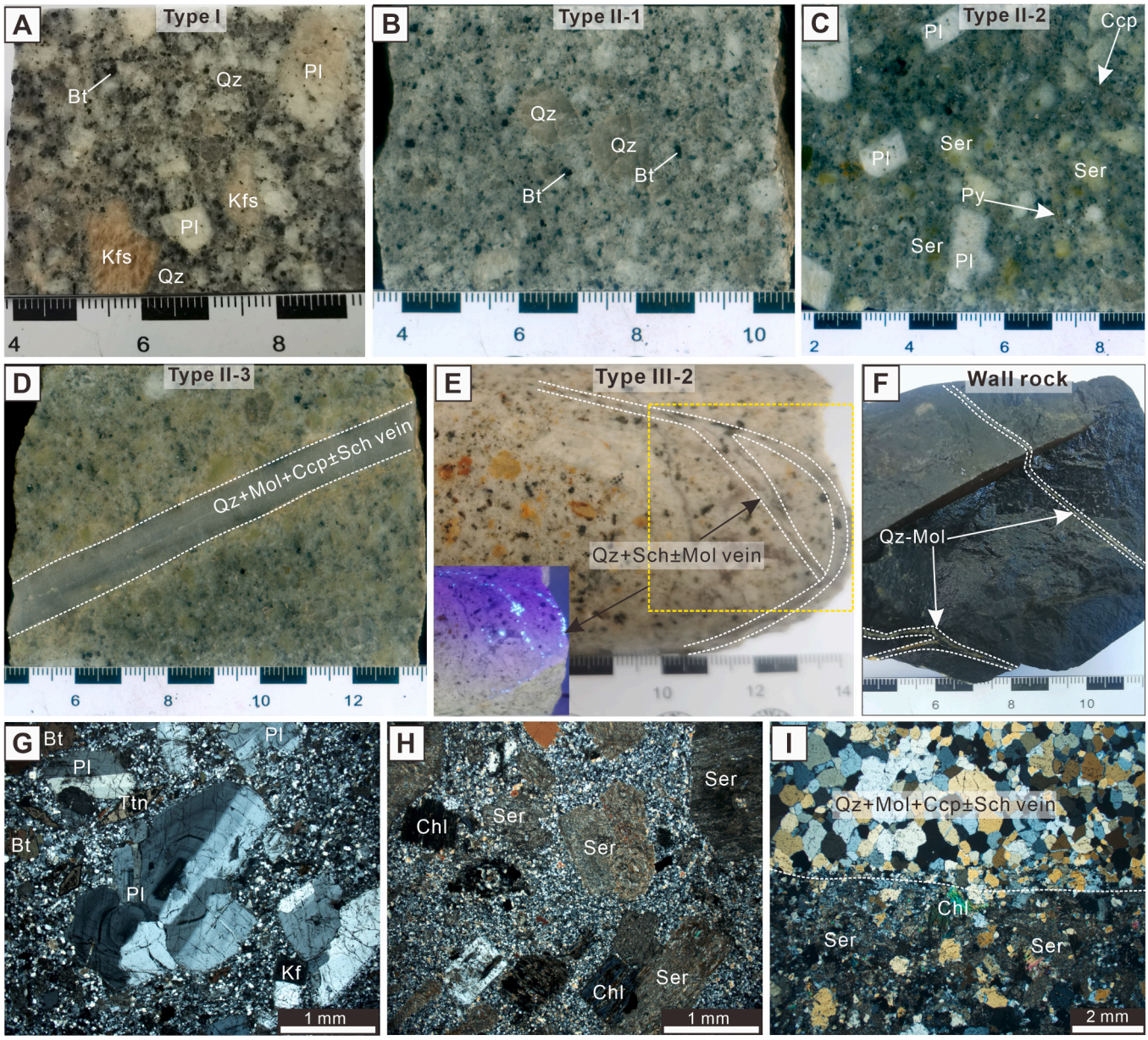

Fig. 3. Photographs of hand specimens and thin sections of different types of porphyries and wall rocks from the Relin deposit. (A) Type I unaltered porphyry; (B) Type II-1 weakly altered Mo–Cu bearing porphyry; (C) Type II-2 moderately altered Mo–Cu bearing porphyry; (D) Type II-3 strongly altered Mo–Cu bearing porphyry; (E) Type II-2 strongly altered W-bearing porphyry. The inset at the lower left corner shows scheelite under fluorescent light; (F) Late Triassic wall rocks (Mo-bearing hornfels); Thin section images (crossed polars); (G) Type I unaltered porphyry; (H) Type II-1 moderately altered Mo–Cu bearing porphyry, plagioclase and biotite are largely altered to sericite and chlorite, respectively; (I) Type II-3 strongly altered porphyry, plagioclase and biotite are nearly completely replaced by sericite, and minor biotite is completely altered to chlorite. Abbreviations: Qz, quartz; Bt, biotite; Kfs, K-feldspar; Pl, plagioclase; Ttn, titanite; Ser, sericite; Chl, chlorite; Mol, molybdenite; Sch, scheelite; Ccp, chalcopyrite; Py, pyrite.

a quartz + molybdenite + chalcopyrite + pyrrhotite ± scheelite vein. Profile P-II (sample ZK10007-79; Fig. 4B) shows moderate to strong alteration from P-II-1 to P-II-4. P-II-5 represents a 5 mm wide alteration halo developed around a quartz + molybdenite-chalcopyrite ± scheelite vein. Profile P-III (specimen ZK10007-84; Fig. 4C) includes three sections of moderate alteration (P-III-1 to P-III-3) and a pyrite + molybdenite + chalcopyrite ± quartz vein (P-III-4). Profile P-IV (sample ZK10007-183; Fig. 4D) shows gradually stronger alteration from weak to moderate (P-IV-1 to P-IV-4). There are two slices (P-IV-5 and P-IV-6) from the mineralized quartz + molybdenite + chalcopyrite + pyrite ± scheelite vein.

The wall rocks of the porphyry typically show only minor alteration. We investigated two samples of weakly altered metasandstone and two samples of Mo-bearing (quartz–molybdenite vein) hornfels (Fig. 3F).

3. Analytical methods and results

Analytical methods and measurement conditions are presented in detail in the Supplementary Material 1.

3.1. Whole rock geochemistry

Major and trace element compositions of porphyry and wall rock samples are listed in Table S1 of Supplementary Material 2. The porphyry samples are metaluminous to weakly peraluminous, with aluminum saturation indexes (A / CNK) of 0.89 to 1.06, indicating I-type

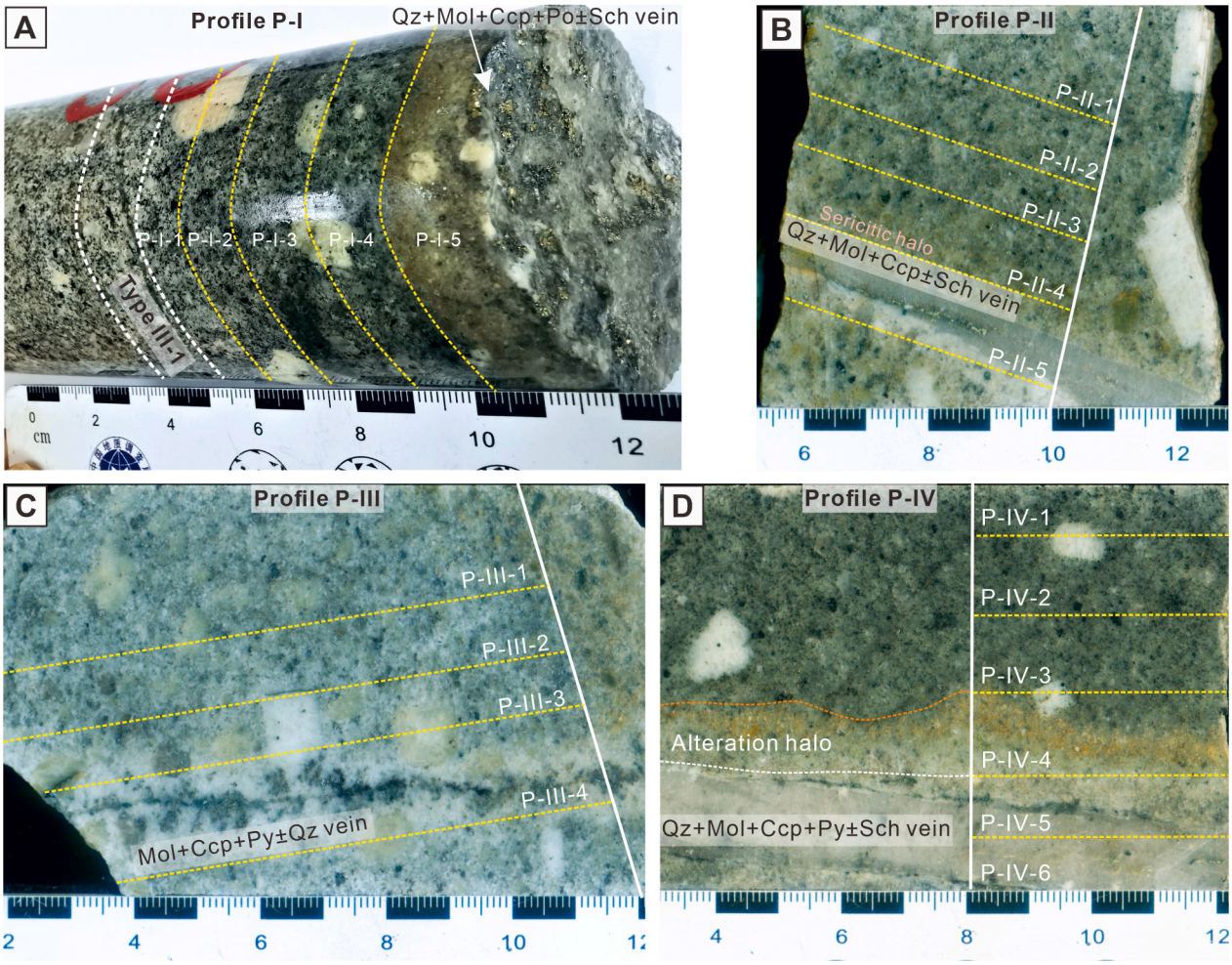

Fig. 4. Photographs of hand specimens of porphyry from four profiles (i.e., P-I, P-II, P-III, and P-IV) from the Relin deposit. (A) Type III-1 weakly altered W-bearing porphyry and Profile P-I showing increasingly stronger alteration from the porphyry to the sulfide-bearing vein; (B) Profile P-II; (C) Profile P-III; (D) Profile P-IV. Labels 1 to (4)-6 refer to increasingly stronger alteration from the unaltered rock to the mineralized vein over a distance of only a few centimeters. Abbreviations are the same as in Fig. 3.

affinity. The fresh Type I and the weakly altered Type II-1 porphyry samples have high SiO_2 (69.6–71.19 wt%) and Al_2O_3 (13.62–14.81 wt %) contents and low Fe_2O_3 (2.39–2.96 wt%), CaO (1.77–2.32 wt%), P_2O_5 (0.15–0.20 wt%), and TiO_2 (0.40–0.46 wt%) contents. The porphyry samples have high total alkali contents ($Na_2O + K_2O = 7.59$ to 8.15 wt%). Sulfur contents range from 0.91 to 1.11 wt%.

The samples except for one strongly altered Type III-2 porphyry plot in the compositional fields of granodiorite, quartz monzonite, and granite (Figs. 5A and Fig. 6A), similar to other collision-related mineralized porphyries in China, i.e., Qulong and Yulong. These porphyry rocks from Relin belong to the high-K calc-alkaline series (Fig. 5B). Fresh Type I and weakly altered Type II-1 porphyry samples plot in the (2Ca + Na + K) / Al vs. K / Al diagram (Fig. 6B) in the granite field. Moderately altered Type II-2 and strongly altered Type II-3 porphyry samples show two kinds of deviation from the granite field. One kind is characterized by higher K / Al values but lower (2Ca + Na + K) / Al values, indicating the addition of K and the loss of Ca and Na. The other kind has higher K/Al and (2Ca + Na + K) / Al values, reflecting variable additions of K, Ca, and Na.

To highlight the compositional changes during alteration, the major element compositions of the altered porphyries (i.e., Types II-1, II-2, II-3, III-1, and III-2) were normalized by the composition of the fresh porphyries (Type I; Fig. S1A in the Supplementary Material 3). Although the extent of alteration seems to differ for the two mineralization types, there are systematic changes with increasing alteration, including lower Fe_2O_3, CaO, Na_2O, MnO, and P_2O_5 contents with stronger alteration and higher K_2O and S contents and loss on ignition (LOI) with stronger alteration. The decrease of the Fe_2O_3, MnO, and CaO contents with stronger alteration reflects the breakdown of biotite and amphibole, whereas the decrease of Na_2O and the increase of K_2O is related to sericitization and potassic alteration of feldspar. The porphyry samples from the profiles P-I, P-II, P-III, and P-IV across Mo–Cu (–W)-bearing veins show similar major element variations (Fig. S1B–E in the Supplementary Material 3) with loss of Fe_2O_3, CaO, Na_2O, P_2O_5, and TiO_2 and increase of K_2O in samples closer to the mineralized quartz veins.

To illustrate the effect of alteration on the trace element contents of porphyry samples, we normalized all samples to the compositions of the average upper continental crust (UCC, Fig. 7A; Rudnick and Gao, 2003) and the altered samples to the fresh porphyry samples (Fig. 7B). All samples have a steeper REE pattern than the UCC and are enriched in Mo, Cu, W, Rb, and Bi, which in part reflects the evolved character of the rocks and the overall high availability of those ore elements that are also enriched in the deposit. Increasing alteration affected some elements preferentially, resulting in systematically lower LREE and Sr contents and higher Rb and Bi contents (Fig. 7B).

The short profiles (Fig. 7C–F) show similar UCC normalized trace element variations as the samples taken on the scale of the entire intrusion, with two important differences: (i) chemical changes among samples taken on the larger scale are not only due to the hydrothermal alteration, but also show the effect of contrasting magmatic

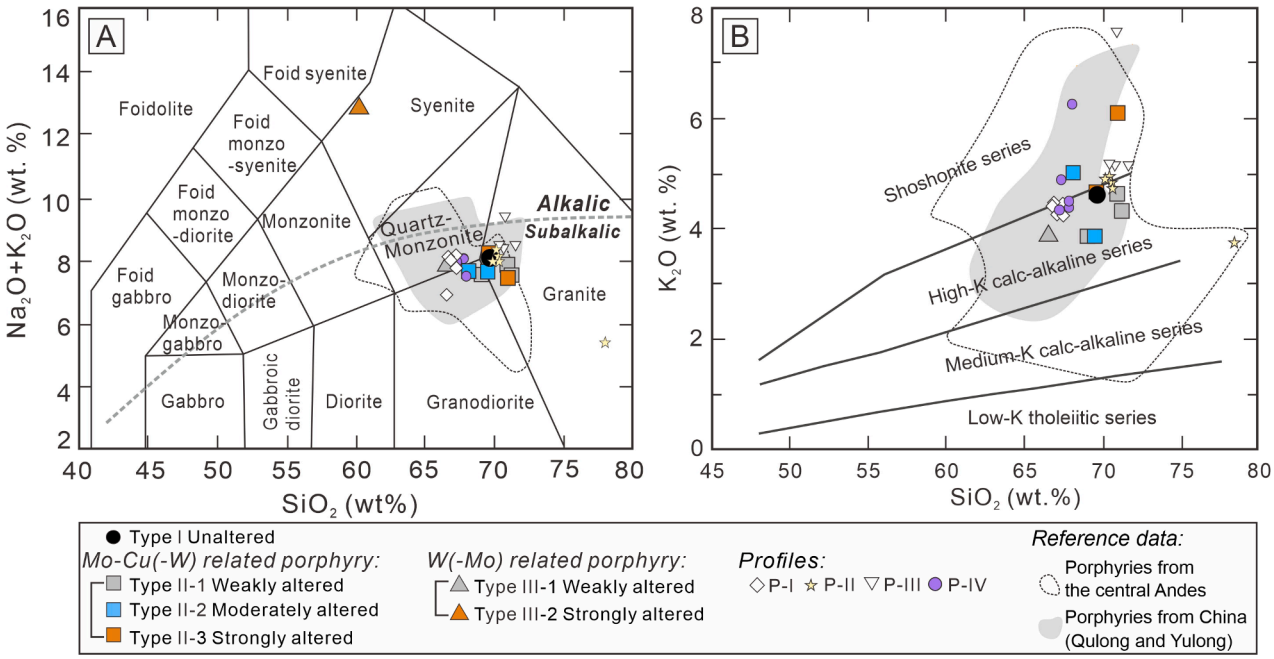

Fig. 5. Major element discrimination diagrams showing unaltered and altered porphyry samples from the Relin deposit. (A) ($Na_2O + K_2O$) vs. SiO_2 diagram (Middlemost, 1994). The analysed samples fall in the range of granodiorite, quartz monzonite, and granite, except for a quartz vein (P-IV-6; Not shown in figure) and a strongly altered sample. (B) In the K_2O vs. SiO_2 diagram (Peccerillo and Taylor, 1976), the porphyries from the Relin intrusion fall in the fields of high-K calc-alkaline to shoshonite series, similar to the collision-related porphyries of the Qulong and Yulong deposits. Data sources for the reference fields: Collision-related porphyries of China (Qulong and Yulong; Yang et al., 2009; Huang et al., 2019); subduction-related porphyries of the central Andes (Stern et al., 2011; Zentilli et al., 2018).

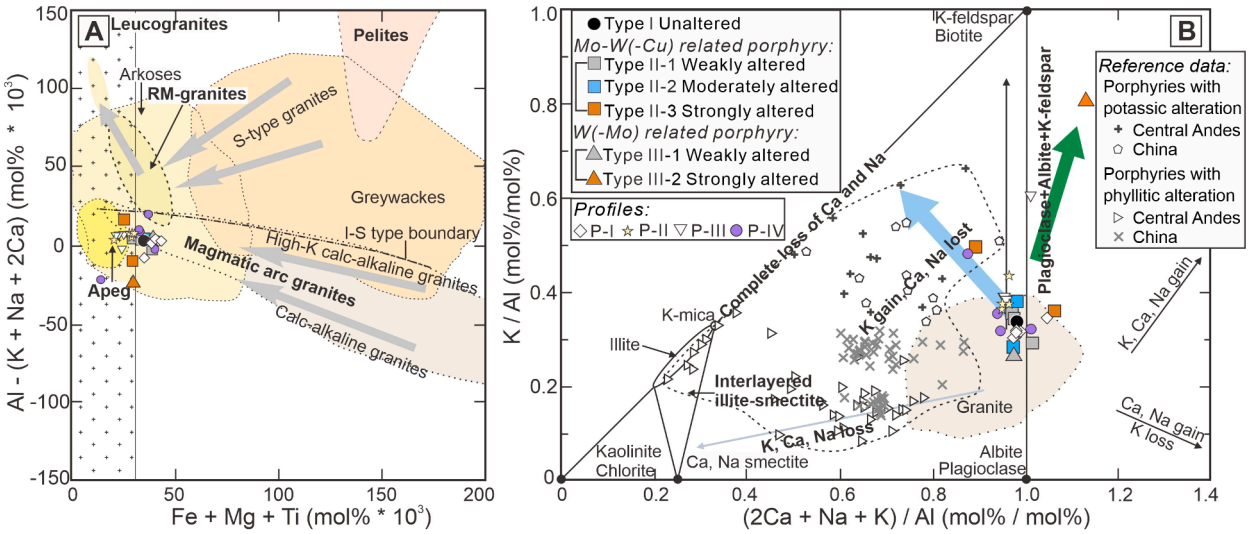

Fig. 6. Major element composition of unaltered and altered porphyry rocks from the Relin deposit. (A) Petrogenetic classification diagram (after Debon and Le Fort, 1983), showing different evolution trends of granite suites. The Relin granites cluster near the highly-evolved end of the calc-alkaline to high-K calc-alkaline suite and fall in the field of I-type granites. (B) The (2Ca + Na + K) vs. K / Al molar element ratio diagram modified after Warren et al. (2007) shows the gain and loss of major elements during the alteration processes. Unaltered Type I and weakly altered Type II-1 porphyry samples plot in the compositional range typical for granite. Moderately and strongly altered porphyry samples define two types of variation trends. One trend (blue arrow) reflects the addition of K and the loss of Ca and Na. This trend is typically found in collision-related porphyry deposits. The other trend (green arrow) is characterized by higher K / Al and (2Ca + Na + K) / Al values with increasing alteration, reflecting variable additions of K, Ca, and Na. Data sources as in Fig. 5. (For interpretation of the references to color in this figure legend, the reader is referred to the web version of this article.)

fractionation, and (ii) the presence of quartz veins reduces the contents of other elements by dilution, which is most obvious in the parallel offset of the normalized REE patterns to lower contents of the profile samples with increasing alteration (Fig. 7C–F).

3.2. Sr–Nd–Pb isotopic compositions

Measured and initial whole-rock Sr–Nd–Pb isotopic compositions are shown in Tables S2 and S3 in the Supplementary Material 2 and presented in Figs. 9 and 10. The initial isotopic compositions of Sr, Nd, and Pb were calculated using the zircon U–Pb age of the porphyry (80 Ma;

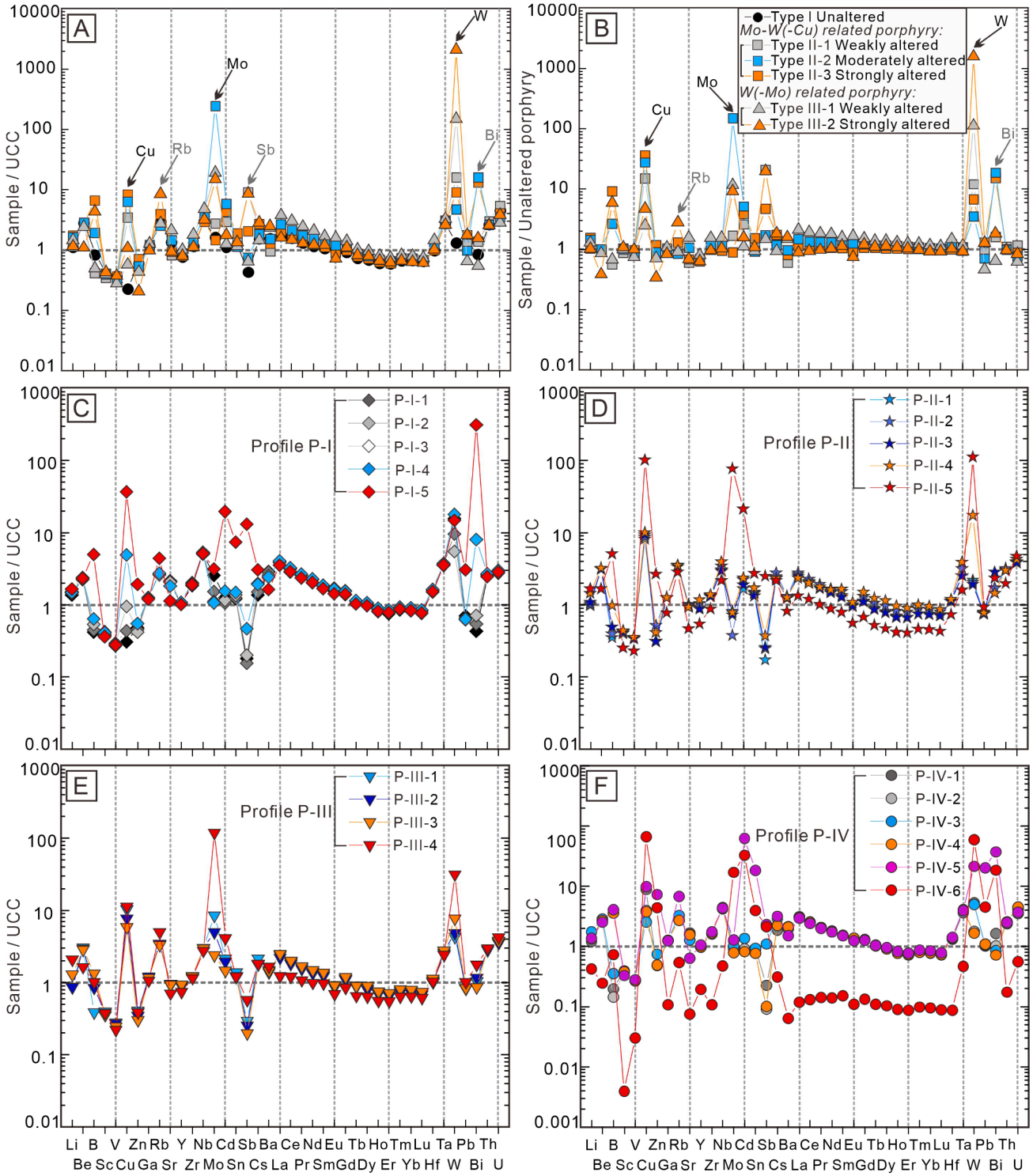

Fig. 7. Trace element variations of fresh and altered porphyry samples from the Relin deposit. Diagrams are normalized by the compositions of the average Upper Continental Crust (UCC; Rudnick and Gao, 2003), except for panel B that shows variably altered porphyries normalized by the composition of fresh porphyry. A. Fresh and altered porphyry samples show steeper REE patterns and are enriched in Mo, Cu, W, Rb, and Bi relative to UCC. B. Trace element compositions of weakly altered to strongly altered porphyry samples normalized to fresh porphyry show significant enrichments in Mo, Cu, W, Rb, and Bi. Note the divergence of the REE pattern with increasing alteration. C–F. Trace element patterns of samples from the four profiles (P-I, P-II, P-III, and P-IV) normalized to the UCC. All samples are characterized by steeper REE patterns and remarkable enrichment of Mo, Cu, W, Rb, and Bi. Note that the vein samples have lower REE contents and higher Mo, Cu, and W contents due to the dilution by quartz and the presence of ore minerals (i.e., molybdenite, chalcopyrite, and scheelite). This dilution effect is particularly obvious for profiles P-II and P-IV.

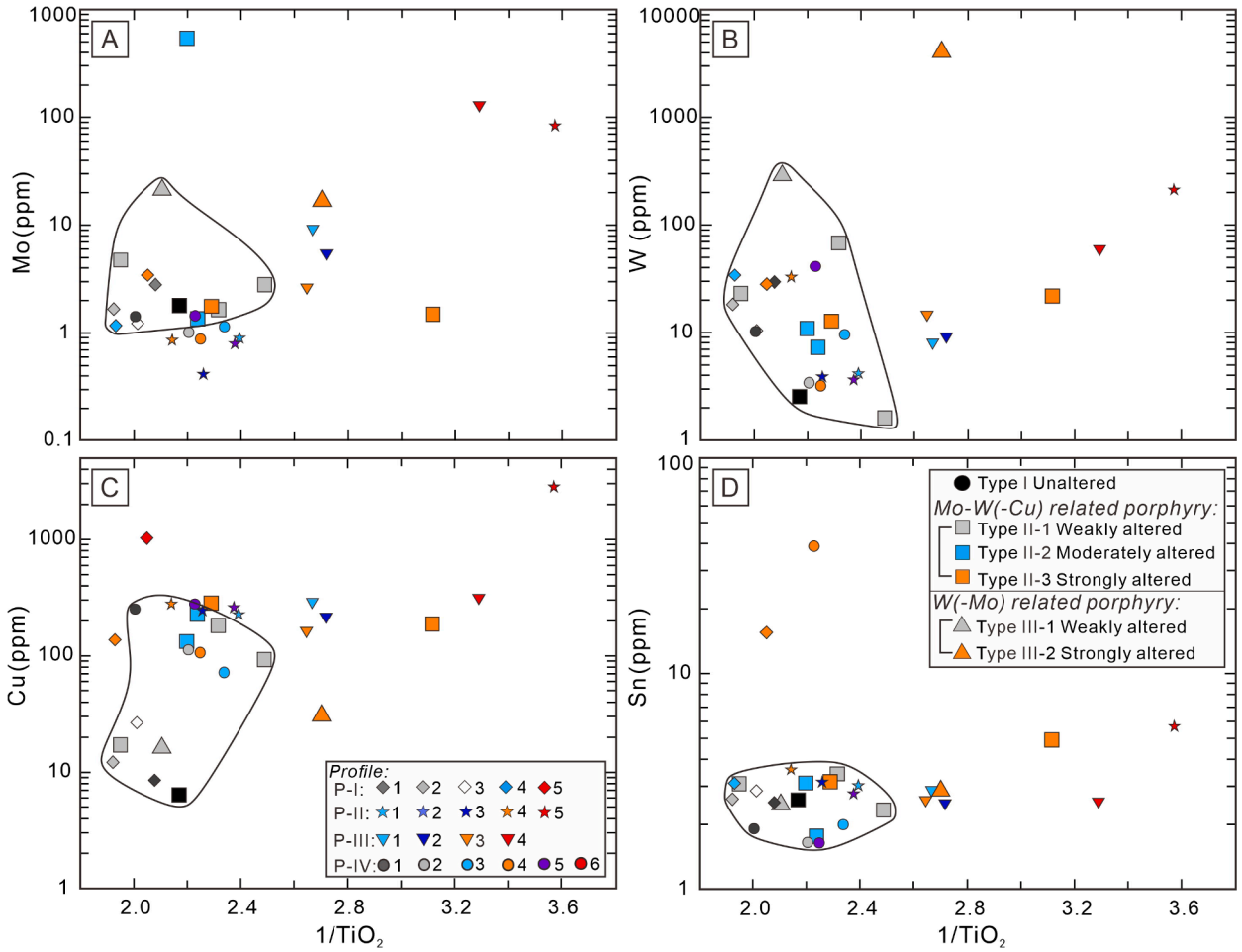

Fig. 8. A–D. Enrichment of ore elements Mo, W, Cu, and Sn during fractional crystallization and hydrothermal alteration. The data of fresh and weakly altered porphyries fall in a relatively narrow field at low $1/TiO_2$ values. The scatter between the Mo, W, Cu, and Sn contents and $1/TiO_2$ of the fresh and weakly altered samples reflects that the enrichment of these ore elements is not controlled by fractional crystallization alone, but is variably affected by redistribution (and/or addition) during hydrothermal alteration. The altered samples may have markedly higher $1/TiO_2$ values, largely reflecting the addition of SiO_2 during alteration, which increases $1/TiO_2$ by dilution.

Gao et al., 2017).

The porphyry samples have initial Nd isotope compositions ranging from –8.6 to –6.6, which corresponds to two-stage Nd model ages (Liew and Hofmann, 1988) ranging between 1367 Ma and 1524 Ma. Note, we report two-stage model ages as the REE pattern of highly evolved granitic rocks may be disturbed by the tetrad effect and extensive late-magmatic fluid-rock interaction and as a result thereof yield highly anomalous single-stage Nd model ages (see Xiang et al., 2020).

The porphyry samples are characterized by relatively unradiogenic initial Sr isotopic compositions, with $^{87}Sr/^{86}Sr_{80}$ ratios of 0.70186–0.71337. Most fresh and altered porphyry samples fall in a narrower range of calculated initial $^{87}Sr/^{86}Sr$ ratios (0.70660 to 0.71028; Fig. 9). A few samples with distinctly lower (0.70186) or higher (0.71337) initial $^{87}Sr/^{86}Sr$ ratios because of secondary changes of the $^{87}Rb/^{86}Sr$ ratios of the rocks. The initial $^{87}Sr/^{86}Sr$ values of four profile samples (i.e., P-I, P-II, P-III, and P-IV) are similar to fresh porphyry, varying between 0.70746 and 0.70930.

In contrast to the porphyry samples, the wall rocks have lower εNd_{80} values of –12.4 to –12.0 that correspond to model ages of 1648 to 1710 Ma and relatively radiogenic $^{87}Sr/^{86}Sr_{80}$ values of 0.72177 to 0.72488 (Fig. 9).

Post-crystallization loss of Pb relative to Th and U may result in over-correction of in situ Pb growth resulting in remarkably low $^{206}Pb/^{204}Pb_{80}$, $^{207}Pb/^{204}Pb_{80}$, and $^{208}Pb/^{204}Pb_{80}$ values, whereas preferential U loss during weathering (e.g., Carpentier et al., 2013) results in under-correction of in situ radiogenic Pb ingrowth and consequently in too high calculated $^{206}Pb/^{204}Pb_{80}$, $^{207}Pb/^{204}Pb_{80}$, and $^{208}Pb/^{204}Pb_{80}$ values (Romer et al., 2022). The $^{206}Pb/^{204}Pb_{80}$, $^{207}Pb/^{204}Pb_{80}$, and $^{208}Pb/^{204}Pb_{80}$ values fall in the range of 17.37 to 18.96, 15.57 to 15.66, 39.10 to 39.51 (Table S2 in the Supplementary Material 2), respectively, which may reflect that the Pb isotopic composition of some samples had been affected by secondary processes. Samples from the four short profiles have $^{206}Pb/^{204}Pb_{80}$, $^{207}Pb/^{204}Pb_{80}$, and $^{208}Pb/^{204}Pb_{80}$ values of 17.20 to 18.78, 15.57 to 15.70, 39.20 to 39.55 (Table S3 in the Supplementary Material 2). Similar to the porphyry samples, the wall rocks also show disturbed initial Pb isotopic values, with $^{206}Pb/^{204}Pb_{80}$, $^{207}Pb/^{204}Pb_{80}$, and $^{208}Pb/^{204}Pb_{80}$ values varying from 17.56 to 18.30, 15.59 to 15.62, 39.30 to 39.67 (Table S2 in the Supplementary Material 2), respectively. As the overcorrection of in situ Pb growth may induce scatter in the Pb isotope diagrams, we decided to plot the measured Pb isotope compositions and discuss the data in terms of initial heterogeneity and in situ growth. Most samples have high $^{207}Pb/^{204}Pb$ values and fall between the average lead evolution curves of orogenic and upper continental crust (Zartman and Doe, 1981), which implies that the Pb budget of these samples is dominated by an old crustal source (Fig. 10A). Furthermore, these samples have relatively high $^{208}Pb/^{204}Pb$ values and plot between the curves for upper and lower crustal Pb evolution (Fig. 10B).

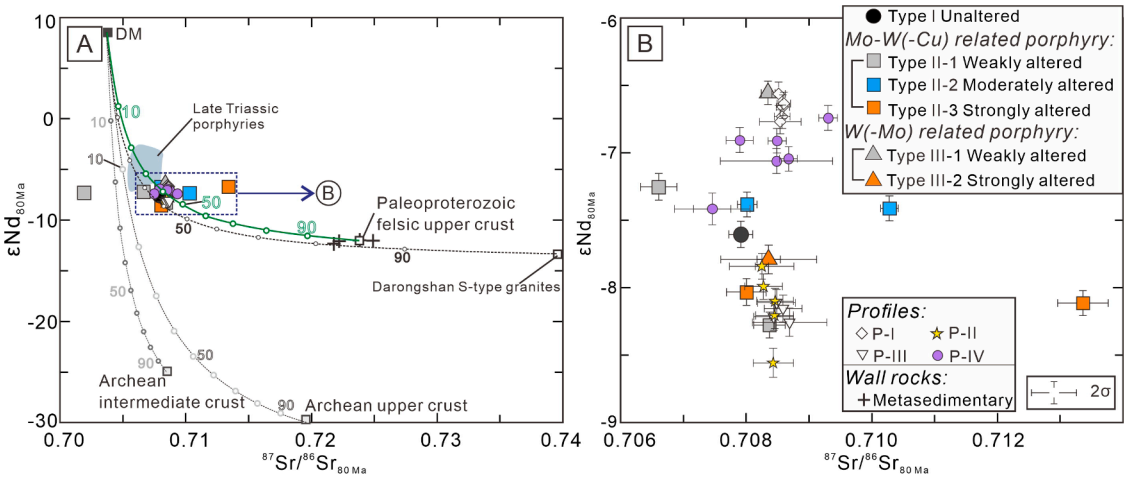

Fig. 9. Whole-rock Sr and Nd isotopic compositions of porphyry and wall rock samples from the Relin deposit. (A) εNd_{80} versus $^{87}Sr/^{86}Sr_{80}$ diagram for variably altered porphyries and their wall rocks. Most of the porphyry samples fall on the binary mixing curve between the mantle and ~ 1.8 Ga old upper crust, except for two samples that have too low and too high $^{87}Sr/^{86}Sr_{80}$ values, respectively. The Rb–Sr systematics of these two samples was disturbed by later processes: The weakly altered sample ZK10007-300 has an anomalously low, over-corrected $^{87}Sr/^{86}Sr_{80}$ value (0.70186) that reflects the increase of the $^{87}Rb/^{86}Sr$ of this sample sometime after the emplacement of the granite, whereas the strongly altered sample ZK10007-107 has a higher $^{87}Sr/^{86}Sr_{80}$ value (0.71337) that reflects a secondary decrease of its $^{87}Rb/^{86}Sr$ ratio. Note, a binary mixing curve between mantle and Archean crust would define a different mixing curve pointing to lower εNd_{80} values. The shown binary mixing curves were calculated for the following end member melts: mantle: Sr = 450 ppm, $^{87}Sr/^{86}Sr_{80}$ = 0.7037, Nd = 7 ppm, εNd_{80} = 9; Paleoproterozoic upper crust: Sr = 190 ppm, $^{87}Sr/^{86}Sr_{80}$ = 0.7238, Nd = 35 ppm, εNd_{80} = –12.0; Archean lower crust: Sr = 300 ppm, $^{87}Sr/^{86}Sr_{80}$ = 0.7085, Nd = 22 ppm, εNd_{80} = –25; Archean upper crust: Sr = 350 ppm, $^{87}Sr/^{86}Sr_{80}$ = 0.7195, Nd = 34 ppm, εNd_{80} = –30. Labels on the binary mixing curve refer to mass fractions (wt.%) of the crust components. Data sources: Late Triassic porphyries in the southern Yidun (Wang et al., 2021); Late Triassic Darongshan S-type granites in South China (Qi et al., 2007). (B) εNd_{80} versus $^{87}Sr/^{86}Sr_{80}$ (±2σ) diagram for the porphyry samples. Most unaltered and altered porphyry samples have calculated $^{87}Sr/^{86}Sr_{80}$ ratios fall in a narrow range between 0.70660 and 0.71028.

3.3. Li–B isotopic compositions

Whole-rock Li and B isotopic data are shown in Tables S2 and S3 in the Supplementary Material 2 and presented in Figs. 11 and 12. The porphyry samples with different degrees of alteration display a narrow range of Li contents (21.1 to 51.1 ppm) and a broad range of δ^7Li values (–6.0 to 11.4 ‰). Type I fresh and Types II-1 and III-1 weakly altered porphyries have Li content of 23.7 to 31.8 ppm and δ^7Li values of –2.3 to 1.5 ‰, i.e., fall in the range of typical I-type granites (δ^7Li: –2.5 to 2.7 ‰; Teng et al., 2004). The Li contents and δ^7Li values of porphyry samples show two trends (Fig. 11A). One trend is characterized by similar δ^7Li values as Type I and II-1 rocks and by a broad range of Li contents. Samples defining the other trend show a significant increase in δ^7Li (–2.3 to 7.8 ‰) with increasing alteration. Samples from the four profiles also show an increase in δ^7Li from the weakly altered distal domains to the mineralization vein (–6.0 to 11.4 ‰). There is no systematic variation between δ^7Li and the fractionation index $1/TiO_2$ (Fig. 12A).

The metasandstone wall rock samples have Li contents in the range of 25.8 to 48.8 ppm) and δ^7Li values ranging from –0.6 to 2.3 ‰, whereas the quartz–molybdenite bearing hornfels samples have Li contents of 45.2 and 53.2 ppm and δ^7Li values of 0.05 and 0.55 ‰.

Type I fresh and Types II-1 and III-1 weakly altered porphyries have a narrow range of $\delta^{11}B$ values (–8.0 to –12.0 ‰; Fig. 11B), which broadly overlaps with the composition of continental crust (–9.1 ± 2.4 ‰; Marschall et al., 2017). There is a marked decrease in $\delta^{11}B$ values from Type I fresh porphyry to Type II-2 moderately and Types II-3 and III-2 strongly altered porphyries from –8.0 to –29.2 ‰. For the profile samples, there is no systematic change in the B content toward the veins, but the $\delta^{11}B$ values decrease toward the ore-bearing veins (–8.9 to –27.4 ‰). Mineralized veins display extremely low $\delta^{11}B$ values (–16.0 to –27.4 ‰). There is no systematic correlation between $\delta^{11}B$ values and $1/TiO_2$ (Fig. 12B).

The $\delta^{11}B$ values of the wall rock samples also show a significant variation. Weakly altered metasandstones have $\delta^{11}B$ values of –6.6 to –5.5 ‰, whereas quartz–molybdenite bearing hornfelses have lower$\delta^{11}B$ values of –14.5 to –10.6 ‰.

The Li and B contents of porphyries generally show a scattered distribution. There is, however, a scattered positive correlation between Li and B contents of fresh and weakly altered porphyries (Fig. 11C). The $\delta^{11}B$ and δ^7Li values of porphyry samples vary along two different trends with changing alteration (Fig. 11D). Fresh and weakly altered porphyries define one trend that is characterized by a small variation in $\delta^{11}B$ but a broad range in δ^7Li values. In contrast, moderately and strongly altered porphyry samples define a trend toward lower $\delta^{11}B$ values and higher δ^7Li values with an increasing degree of alteration.

4. Discussion

4.1. Chemical variations by fractional crystallization, fluid exsolution, and hydrothermal alteration

The porphyries in the Relin deposit have experienced fractional crystallization and post-magmatic alteration. These processes affected the chemical compositions of the porphyry rocks in different ways. During fractional crystallization, major element contents are affected by the crystallizing minerals, whereas the trace elements are controlled by their partitioning between the crystallizing phases and the melt (Moyen et al., 2021). During late-stage exsolution of a fluid phase, elements will partition between melt and fluid, depending on melt and fluid composition, as well as the availability of ligands (e.g., Heinrich, 1990; Audétat et al., 2008; Schmidt et al., 2020). Finally, chemical changes due to the hydrothermal alteration are controlled by the composition of the altered phases and by the proportion of elements released during alteration, by the balance between incorporation of these elements into secondary phases and their loss into fluids, and last but not least by the potential incorporation of fluid-advected material into the altered rock (Byrne et al., 2020). To identify which elements were affected in different ways during alteration, the initial variation due to fractionation processes has to be assessed first.

Harker diagrams (i.e., major element oxides vs. SiO_2) are widely used to evaluate fractionation trends, but are not very useful for highly evolved granite samples (Moyen et al., 2021) that may crystallize

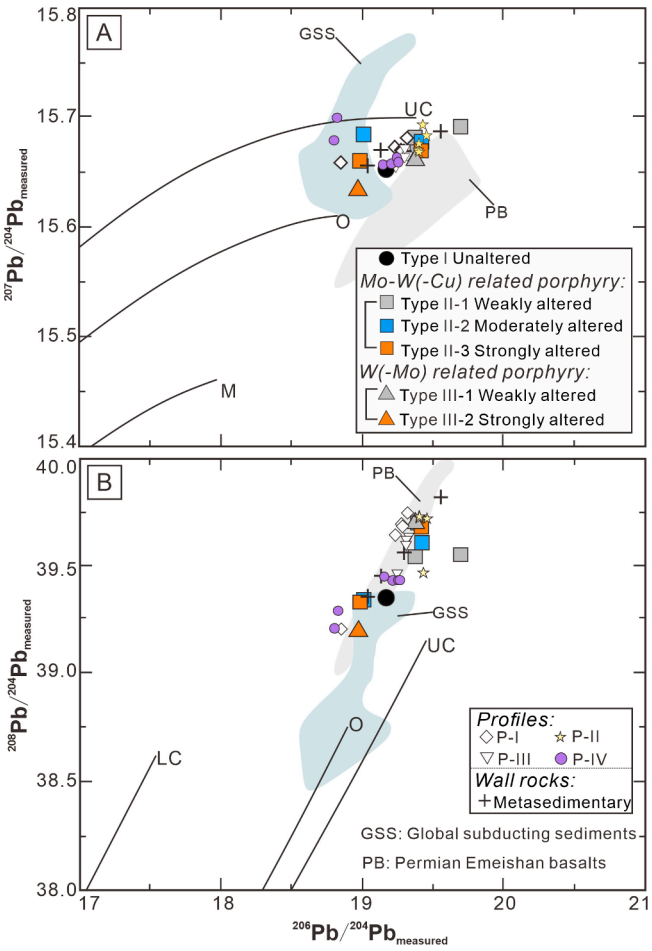

Fig. 10. Measured Pb isotopic ratios for variably altered porphyries and wall rocks from the Relin deposit. (A) In the $^{207}Pb/^{204}Pb$ vs. $^{206}Pb/^{204}Pb$ diagram, porphyry and wall rock samples fall between the upper crust (UC) and orogen (O) evolution curves; (B) In the $^{208}Pb/^{204}Pb$ vs. $^{206}Pb/^{204}Pb$ diagram, porphyry and wall rock samples are slightly offset toward the evolution curve of the lower crust (LC). As both intense chemical weathering and high-grade metamorphism result in major loss of U and Pb, rocks having experienced these processes develop with time Pb isotopic compositions with LC characteristics (e.g., Franz et al., 2013; Romer and Hahne, 2010). The shift of the data from the Relin porphyry toward the LC Pb evolution curve may reflect the involvement of ancient, sedimentary rocks from deeply weathered crustal rocks rather than the involvement of ancient lower crust. Data sources: Curves for average lead evolution (Zartman and Doe, 1981); Global subducting sediments (GSS; Plank and Langmuir, 1998); Permian Emeishan basalts in the western Yangtze Block (PB; Fan et al., 2008). Abbreviations for Pb evolution curves: UC = upper crust, O = orogene, M = mantle, LC = lower crust.

fluorite, muscovite, and cordierite, which reduces bulk-rock SiO_2 contents. As TiO_2 remains largely immobile during a wide range of alteration processes, $1/TiO_2$ can be used as a fractionation index (e.g., Förster et al., 1999). Correlation between major and trace elements contents and the fractionation index ($1/TiO_2$) reflect fractional crystallization (Fig. S2 in the Supplementary Material 3). Most fresh and altered porphyry samples fall on trends that reflect fractional crystallization, implying that magmatic fractionation largely controlled the whole-rock compositions of the Relin porphyries. The negative correlation of major elements (e.g., Fe_2O_3, MgO, Al_2O_3, CaO, and Na_2O) and trace element ratios (Rb/Sr) with $1/TiO_2$ (Fig. S2A–F in the Supplementary Material 3) reflects the fractional crystallization of mafic minerals (i.e., biotite and amphibole), plagioclase, and accessory titanite. Similarly, the negative correlations of P_2O_5 with $1/TiO_2$ (Fig. S2G in the Supplementary Material 3) indicate fractional crystallization of accessory apatite. Some elements and element ratios e.g., Na_2O and Rb/Sr, deviate from the fractionation trend (Fig. S2E–F in the Supplementary Material 3), indicating that later alteration processes resulted in lower Na_2O contents and significantly higher Rb/Sr ratios. These chemical changes basically reflect the alteration of the original feldspar. The scattered distribution between ore elements (Mo, W, Cu, and Sn) and $1/TiO_2$ (Fig. 8) reflects that the enrichment of these elements is related to alteration rather than fractional crystallization.

Late-stage exsolution of a fluid phase partitions elements between melt and fluid. This process may deplete the melt in particular in those elements that strongly partition into the fluid, as for instance B (e.g., Schatz et al., 2004) and some ore elements (e.g., Heinrich, 1990; Audétat et al., 2008; Schmidt et al., 2020). The loss of incompatible elements to the fluid actually may account for the scatter of some ore elements in Harker-type diagram (Fig. 8). The fluid eventually transports those elements that strongly partition into the fluid from the intrusion to the apical parts and the wall rocks of the intrusion, where they may form mineralization and alteration haloes.

There are three petrographically discernable types of alteration by hydrothermal fluids in the Relin deposit: (i) weak potassic alteration of feldspar, (ii) sericitization of plagioclase, and (iii) replacement of biotite and amphibole by chlorite and carbonate. Increasing intensity of alteration results in the superposition of the various alteration types. Compared with typical subduction-related deposits in the Andean belt and collision-related porphyry deposits in China (i.e., Qulong and Yulong), the Relin deposit shows a low degree of alteration and relatively minor alteration-related geochemical variations. Hydrothermal alteration is not pervasive but seems to be bound to centimeter- to decimeter-wide zones bordering mineralized quartz veins (Fig. 4).

Mass transfer related to hydrothermal alteration has been quantitatively evaluated using Isocon analysis (Gresens, 1967; Grant, 2005; López-Moro, 2012). The results of this calculation are shown and discussed in the Supplementary Material 1. In the text below, we illustrate the progressive chemical changes by normalizing the compositions of the rocks in variation diagrams, making losses and gains visible as troughs and peaks, respectively (Fig. 7).

Relative to the UCC, all porphyry samples show variable enrichment of Mo, Cu, W, Rb, and Bi (Fig. 7A). Profile samples show similar distribution patterns as fresh porphyry samples (Fig. 7C–F), whereas vein samples with abundant quartz and ore minerals (i.e., molybdenite, chalcopyrite, and scheelite) have lower REE contents but higher contents of Mo, Cu, W, and Sn.

By normalizing to fresh Type I porphyry (Fig. 7B), rare earth and trace elements of porphyry samples display different mobility from weakly altered porphyry to strongly altered porphyry. Most elements from Types II (II-1, II-2, and II-3) and III (III-1, and III-2) remain immobile, whereas the breakdown of feldspar and its replacement by secondary sericite resulted in a significant decrease of Sr and an increase in Rb. Lithium contents basically remained unchanged during weak alteration, but shows small gains in moderately altered Type II-2 porphyry and strongly altered Type II-3 porphyry. Boron shows slight loss in Type II-1 and Type III-1weakly altered porphyries and variable gains in Type II-2 moderately altered and Types II-3 and III-2 strongly altered porphyries, reflecting that the composition of the fluid was changed by progressive alteration of porphyries and/or that different fluid sources became available over time. Fluid-induced alteration leads to significant enrichment of incompatible elements Mo, Cu, and W and chalcophile element Bi in all alteration stages. The contents of Mo, Cu, and Bi systematically increase from Type II-1 weakly altered porphyry to Type II-3 strongly altered porphyry. The contents of W also increase from Type III-1 weakly altered porphyry to Type III-2 strongly altered porphyry. The rocks have only low Sn contents. The little Sn present seems to have been redistributed in strongly altered Type II-3 porphyry and in part may have been mobilized from weakly and moderately altered porphyries. These observations indicated that alteration processes were more important than fractional crystallization for the enrichment of sulfur and

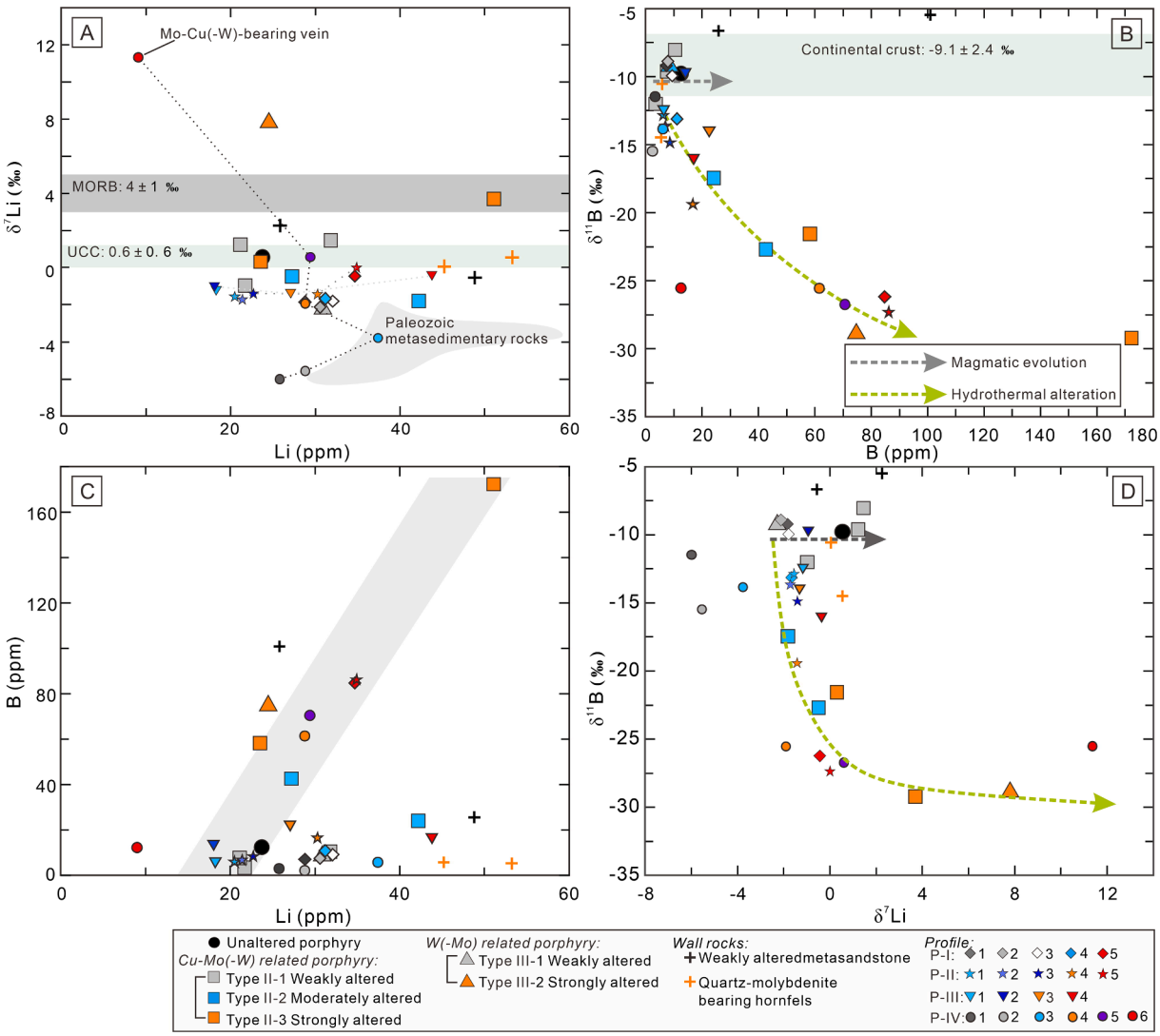

Fig. 11. Variation of Li and B isotopic compositions for porphyries and wall rock samples from the Relin deposit. A. δ^7Li vs. Li (ppm). Dotted line shows the pieces from weakly altered P-IV-1 to vein P-IV-6. The Li isotope compositions of most samples fall in a group with a relatively narrow range of δ^7Li values (–2.27 to 1.45 ‰) and a wide range of Li concentrations (18.1 to 53.2 ppm). Samples with distinctly higher δ^7Li values experienced major hydrothermal alteration or represent quartz veins with variable amounts of ore minerals, whereas porphyry samples with distinctly lower δ^7Li values (–3.8 to –6.0 ‰) reflect contributions from nearby metasedimentary rocks. B. δ^{11}B vs. B (ppm). The B contents and δ^{11}B values define two trends. One trend shows a narrow range of δ^{11}B values (–8.03 to –9.77 ‰) and a broad range of B contents (6.73 to 102 ppm). As B behaved mostly incompatibly during magmatic evolution, B contents increase without significant change in δ^{11}B. The second trend defines a mixing hyperbola from fresh or little altered granites (low B content) to low δ^{11}B values at high B contents. This mixing hyperbola reflects B additions during hydrothermal alteration. C. B contents (ppm) vs. Li contents (ppm). Fresh and little altered porphyries seem to show an overall correlation between Li and B contents. Alteration generally seems to add to variable extent Li and B. D. δ^{11}B vs. δ^7Li values. The δ^{11}B and δ^7Li values of variable altered porphyry samples plot in two trends. One trend shows similar δ^{11}B but variable δ^7Li values in the weakly and moderately altered porphyries. The other trend shows a systematic decrease of δ^{11}B values and increase of δ^7Li values with stronger alteration. Reference fields: Average δ^7Li composition: upper continental crust (UCC) (Teng et al., 2004), MORB (Tomascak et al., 2008); Paleozoic sedimentary rocks from the Erzgebirge, Germany (Romer and Meixner, 2014). Average δ^{11}B composition of bulk continental crust (Marschall et al., 2017).

metal elements (Cu, Mo, W, and Sn).

4.2. Source signatures of the Relin porphyries

Although the porphyry and wall rock samples from the Relin deposit experienced various degrees of alteration, the εNd_{80} values of the various samples fall in a narrow range, whereas the corresponding $^{87}Sr/^{86}Sr_{80}$ values define a broader range. The data scatter about a binary mixing curve in the εNd_{80} vs. $^{87}Sr/^{86}Sr_{80}$ diagram (Fig. 9A). Binary mixing trends (Fig. 9A) involving typical crustal and mantle end members indicate that crustal contributions to the Relin intrusions mainly originate from early Proterozoic source rocks (εNd_{80} –11 to –15). The involvement of Archean sources would result in a trend to distinctly lower εNd_{80} values (Fig. 9A). The early Proterozoic crustal component could be either the old crust or younger sediments that were derived from an early Proterozoic craton. Published Hf–O isotope data from zircon (εHf_{80} = –12.1 to –2.1; $\delta^{18}O$ = 5.8 to 7.3 ‰; Wang et al., 2014b; Gao et al., 2017) support the contribution of both crustal and mantle sources. The evolved character of the Late Cretaceous Relin porphyry intrusion reflects a sequence of processes, starting with the emplacement of mantle melts in the Paleoproterozoic crust leading to crustal melting and magma mixing and continuing with fractional crystallization of the hybrid melts.

Late-magmatic and hydrothermal alteration may affect the Nd and Sr isotopic compositions by adding Nd and Sr from a reservoir with a different isotopic composition. The small range in εNd_{80} values and the

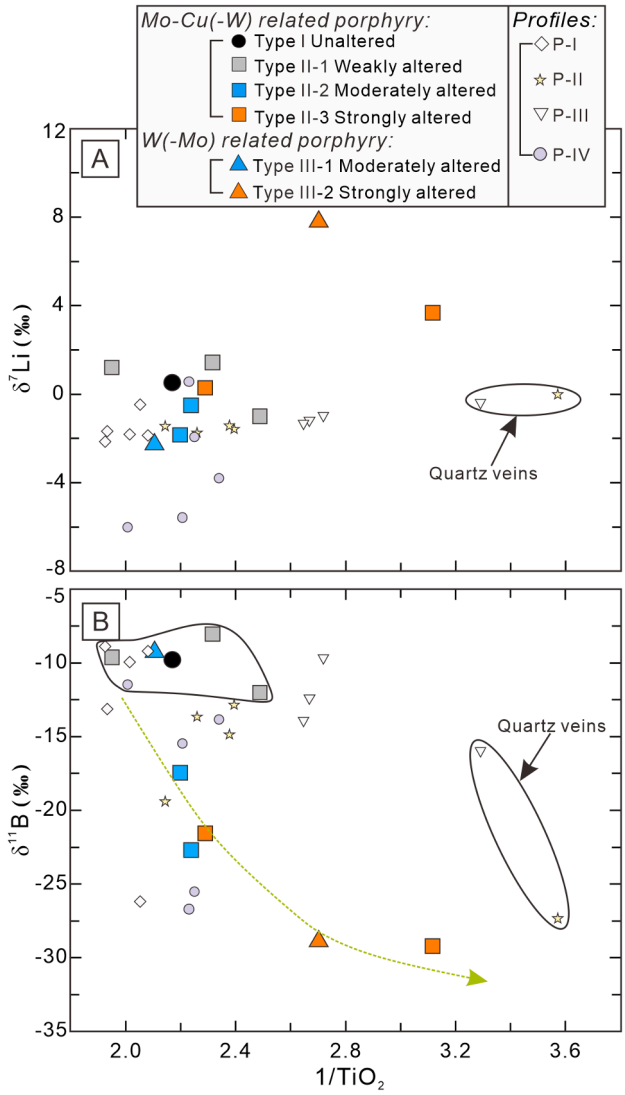

Fig. 12. Variation of Li and B isotopic compositions with $1/TiO_2$ for porphyries and wall rock samples. A. Fresh and little altered samples show no correlation of δ^7Li with $1/TiO_2$ reflecting that fractional crystallization did not cause significant changes in the Li isotopic compositions. B. Fresh and little altered samples show no correlation of $\delta^{11}B$ with $1/TiO_2$. In contrast, a few strongly altered samples show a systematic decrease of $\delta^{11}B$ with higher $1/TiO_2$. As $\delta^{11}B$ is reduced during alteration, this correlation indicates that the precipitation of quartz also affected $1/TiO_2$ by diluting the Ti contents. This dilution effect is particularly obvious for the quartz–sulfide veins from profiles P-II and P-III.

low solubility of REE in aqueous fluids indicates that the observed εNd_{80} values represent the magmatic signature. Samples from the various profiles show only minor εNd_{80} variation, which indicates that Nd isotopic compositions were not affected significantly by alteration, whereas the larger variation in εNd_{80} ofsamples collected on a larger scale reflect regional differences in magma sources and/or AFC processes (Fig. 9). In contrast, the broad range in $^{87}Sr/^{86}Sr_{80}$ values may reflect the broader range of Sr isotopic composition of the melts, addition of Sr, or changes of $^{87}Rb/^{86}Sr$ during alteration. Initial heterogeneity of $^{87}Sr/^{86}Sr_{80}$ or addition of Sr cannot be ruled out, except for one sample with an anomalous low $^{87}Sr/^{86}Sr_{80}$ value (Fig. 9A). Changes of $^{87}Rb/^{86}Sr$ during late-stage alteration has no effect on the calculated $^{87}Sr/^{86}Sr_{80}$ value, whereas changes of $^{87}Rb/^{86}Sr$ during much younger alteration inevitably will result in undercorrection or overcorrection of in situ ^{87}Sr production, i.e., yield too high or too low calculated apparent $^{87}Sr/^{86}Sr_{80}$ values, respectively.

Note, Late Triassic porphyries related to Cu (–Mo) mineralization (e.g., Pulang, Fig. 1) in the Yidun terrane have lower initial $^{87}Sr/^{86}Sr$ values and higher εNd_{80} values than the Relin porphyry (Fig. 9A), which indicates that these rocks contain higher portions of mantle material or juvenile crust (Wang et al., 2019). The corresponding two-stage Nd model ages of the Late Triassic porphyries range from 1.0 Ga to 1.3 Ga.

Due to the contrasting geochemical behavior of U, Th, and Pb during melt extraction from the mantle, high-grade metamorphism, and chemical weathering, the Pb isotopic compositions of different reservoirs (mantle, lower crust, upper crust) evolve over time to different values that provide constraints for the source of melts or sediments. High $^{207}Pb/^{204}Pb$ values at a given $^{206}Pb/^{204}Pb$ are typical for the involvement of ancient crust (Zartman and Doe, 1981). High $^{208}Pb/^{204}Pb$ values at relatively low $^{206}Pb/^{204}Pb$ values are typically found in rocks that have experienced loss of U relative to Pb and Th. As such loss is known to occur during high-grade metamorphism, this Pb isotope signature commonly is interpreted to reflect ancient high-grade metamorphism (Zartman and Doe, 1981). Similar fractionation of U, Th, and Pb, however, may also occur during intense chemical weathering (Franz et al., 2013). The breakdown of feldspar allows for the loss of Pb and the oxidizing environment results in the loss of U relative to Th, eventually with time resulting in Pb isotopic compositions with high $^{208}Pb/^{204}Pb$ at low $^{206}Pb/^{204}Pb$ ratios (Franz et al., 2013). Therefore, the offset of the Pb isotopic compositions toward the LC growth curve (Fig. 10B) does not necessarily involve rocks that experienced an ancient high-grade metamorphic event, but may reflect contributions from old, intensely weathered sedimentary rocks from a crustal source. We interpret the high $^{207}Pb/^{204}Pb$ and $^{208}Pb/^{204}Pb$ values of Relin porphyries (Fig. 10) to reflect the involvement of old sedimentary rocks whose source had experienced strong chemical weathering.

4.3. Sources of the ore fluids

The Li and B isotopic compositions of most porphyry samples from the Relin deposit show no correlation with $1/TiO_2$ (Fig. 12), which implies that fractional crystallization had a limited effect on the whole rock Li and B isotopic fractionation. This insignificant fractionation of Li and B during magma differentiation is also constrained by previous studies (see Tian et al., 2022; Xiang et al., 2020). Note, there may be significant differences among the δ^7Li and $\delta^{11}B$ values of minerals from the same sample due to Rayleigh fractionation during crystallization (see Lei et al., 2023). The absence of large variations in δ^7Li and $\delta^{11}B$ values during fractional crystallization (Fig. 12) essentially reflects that the rock did not experience major loss of Li and B via a melt or fluid after crystallization had started.

Lithium is not completely incompatible during crystallization and, therefore, the remaining melt will develop to higher δ^7Li values as crystallization progresses. The δ^7Li values of late-stage melts and concomitantly of fluids exsolved from such melts are much higher than those of less evolved rocks (e.g., Lei et al., 2023; Magna et al., 2016; Phelps and Lee, 2022). Therefore, pegmatites have much higher δ^7Li values than most granites (e.g., Magna et al., 2010). Boron behaves slightly differently. Boron is rather incompatible during magma development. Therefore, only little B is extracted from I-type melts during crystallization and the $\delta^{11}B$ value of the remaining melt is not changing significantly. The exsolution of a fluid will partition most B into the fluid (Schatz et al., 2004) and reduce $\delta^{11}B$ values of the remaining melt (Trumbull et al., 2013). The difference in $\delta^{11}B$ values between melt and fluid depends on the coordination of B in fluid and melt, as well as on the temperature. For a magmatic system, the offsets may be in the range of 2–6 ‰ (Trumbull et al., 2013; Xiang et al., 2020). As magmatic fluids have higher $\delta^{11}B$ values than the fresh porphyries and the altered rocks, magmatic fluids can account for the alteration of those samples that have higher $\delta^{11}B$ values than the granites, but not for the alteration of the intensely mineralized samples that have $\delta^{11}B$ values that are as much as 15 ‰ lower than those of the granites (Fig. 12B).

Hydrothermal alteration, however, may account for significant variation in the Li and B isotopic compositions of the altered rocks, in part due to addition or loss of fluid-mobile Li and B from the rocks, in part due to the fractionation of the Li and B isotopic compositions between minerals and fluids, with fluids generally having higher δ^7Li and δ^{11}B values than the minerals with which they have equilibrated (Wunder et al., 2007). The Li and B budgets of the rock commonly are dominated by different minerals. Therefore, the isotopic compositions of Li and B may change to a contrasting extent during alteration processes, depending on the stability of the major Li and B hosts and the nature of the altered minerals. For instance, tourmaline, a major host of B and a minor host of Li, is much more resistant to alteration than biotite or muscovite, major hosts of Li and moderate or minor hosts of B. After alteration of rocks containing micas and tourmaline, the δ^7Li values may record this alteration, whereas δ^{11}B values may remain essentially unaffected (Romer et al., 2022).

The δ^7Li and δ^{11}B values of fresh and altered porphyries basically follow two evolution trends. One trend defined by Type I fresh and Types II-1 and III-1 weakly altered porphyries showing variable δ^7Li values at essentially identical δ^{11}B values. The data defining this trend mostly fall in the range typical for the continental crust and may reflect the magmatic evolution of the porphyries (Fig. 11D). Three weakly altered porphyry samples (P-IV-1 to P-IV-3) collected near the contact to the wall rocks of the intrusion have lower δ^7Li values (–3.8 to –6.0 ‰) than Type I fresh and Types II-1 and III-1 weakly altered porphyries. There are two processes that can explain the Li isotopic compositions of these three samples, i.e., additions of Li from a fluid with low δ^7Li values or loss of Li to a fluid. For instance, as metasedimentary rocks generally have low δ^7Li values (–2.0 to –6.1 ‰), depending on source and weathering history of the source (e.g., Qiu et al., 2009; Romer et al., 2014b), fluids originating from such rocks also have relatively low δ^7Li values.

Similarly, the replacement of a primary mineral results in the redistribution of Li contained in this mineral. Whereas simple dissolution of the primary mineral does not fractionate the isotopic composition of the released Li, the partitioning of Li between the fluid and the secondary mineral will result in isotopic fractionation. The secondary mineral will have lower δ^7Li values than the fluid with which it equilibrated. Thus, if some Li released from the primary mineral is lost to the fluid (and leave the system), altered rocks will have lower δ^7Li values than their precursors. The second trend is characterized by a significant shift to higher δ^7Li and lower δ^{11}B values in moderately (Type II-3) to strongly altered porphyry samples (Types II-3 and III-2). This shift is related to the interaction of these rocks with fluids. Magmatic fluids are expected to have higher δ^7Li and δ^{11}B values than the magmatic minerals of the same intrusion and, therefore, the fluids accounting for the second trend in the δ^7Li and δ^{11}B diagram are likely to represent external, wall-rock-derived fluids (Romer et al., 2014a; Xu et al., 2021b). Anomalously high δ^7Li values are observed for the quartz–chalcopyrite–molybdenite–scheelite vein from profile IV and for moderately (Type II-2) and strongly altered porphyry samples (Types II-3 and III-2). Abnormally low δ^{11}B values (down to –29.20 ‰) are observed for moderately (Type II-2) and strongly altered (Types II-3 and III-2) porphyry samples and vein samples. Such high δ^7Li are known from lacustrine sediment and evaporite deposits from playa basins, USA (–1 to 8 ‰; Araoka et al., 2014), continental thermal fluids (1 to 17 ‰; Tomascak, 2004), and saline groundwater (7 to 31 ‰; Tomascak, 2004), whereas low δ^{11}B values are known from non-marine evaporites (Slack et al., 1989). Thus, the very high δ^7Li and very low δ^{11}B values of altered porphyry whole rock samples from the Relin deposit may reflect that the fluids originated from the sedimentary wall rocks of the porphyry intrusions. As very low δ^{11}B values are found in samples with significant enrichment of Cu, W, Mo, and Sn (Fig. 7), these elements were redistributed by external fluids. The ore elements may derive from the source of the fluids or any rock that had interacted with these fluids, including the porphyry.

5. Conclusions

Relin Mo–W (–Cu) mineralization is related to Late Cretaceous intracontinental porphyries. Most fresh and weakly altered porphyry samples have uniform εNd_{80} values (–8.3 to –6.6) and initial $^{87}Sr/^{86}Sr$ ratios (0.70660 to 0.71028). The Sr and Nd isotopic composition of these rocks falls on a binary Sr–Nd mixing curve between mantle-derived melts and Paleoproterozoic crust, implying that the Relin prophyries are derived from hybrid melts that experienced extensive fractional crystallization. Locally, the porphyries show important late-stage hydrothermal alteration and veining with associated mineralization. The metaluminous to weakly peraluminous porphyries show I-type affinity and are characterized by δ^7Li values of –2.3 to 1.5 ‰, and δ^{11}B values of –8.0 to –12.0 ‰. These Li and B isotope compositions reflect the magmatic system. Alteration of the porphyries resulted in variable sericitization that is associated with significant loss of Na_2O and Sr and variable gain of Rb as well as locally important enrichment of the ore elements Cu, Mo, W, Sn, and Bi. Alteration also resulted in the local redistribution of Li and B within the granites and the addition of Li and B through the fluid. The δ^7Li values of altered porphyries fall in the range –6.0 to 11.4 ‰ with the molybdenite-quartz veins having the highest values. The boron contents decrease slightly during weak alteration and increase markedly during moderate and strong alteration. The δ^{11}B values of altered samples decrease systematically with higher intensity of alteration from –12.4 to –29.2 ‰. The anomalously high δ^7Li and low δ^{11}B values reveal the addition of external fluids sourced from the Late Triassic sedimentary wall rocks. These fluids interacted with the porphyries resulting in the remobilization and (minor) addition of the ore elements Mo, W, Cu, and Sn.

Declaration of Competing Interest

The authors declare that they have no known competing financial interests or personal relationships that could have appeared to influence the work reported in this paper.

Data availability

Data will be made available on request.

Acknowledgments

We thank Tao Dong and Haijun Yu (Yunnan Institute of Geological Survey, Kunming), Xuelong Liu and Xiaojun Jiang (KMUST, Kunming), Lili Jiang (Chengdu Center of China Geological Survey, Chengdu), and Xiaoyu Wang (CUG, Wuhan) who helped with the field work and sampling. We also appreciate the kind help of Wanhua Cheng for thin section preparation, Bo Zhou and Shuqin Yang (CAS, Guiyang) for whole-rock major and trace element analyses, and Bettina Hübner (GFZ) for Sr, Nd, Pb, Li, and B isotope analyses. We gratefully acknowledge helpful suggestions by chief editor Huayong Chen and two anonymous reviewers. This research was cooperatively supported by the Selection Project of High-level Scientific and Technological Talents and Innovative Teams Project in Yunnan Province (202305AT350004), the Major Scientific and Technological Projects in Yunnan Province (202202AG050006), the National Key R&D Program of China (2021YFC2901803), and the Open Research fund of State Key Laboratory of Ore Deposit Geochemistry (201803). The work of Fucheng Yang at GFZ was supported by a CSC student scholarship (202106400049).

Appendix A. Supplementary data

Supplementary data to this article can be found online at https://doi.org/10.1016/j.oregeorev.2023.105761.

References

Araoka, D., Kawahata, H., Takagi, T., Watanabe, Y., Nishimura, K., Nishio, Y., 2014. Lithium and strontium isotopic systematics in playas in Nevada, USA: constraints on the origin of lithium. Miner. Deposita 49, 371–379.

Audétat, A., Pettke, T., Heinrich, C.A., Bodnar, R.J., 2008. Special paper: the composition of magmatic-hydrothermal fluids in barren and mineralized intrusions. Econ. Geol. 103, 877–908.

Barra, F., Ruiz, J., Valencia, V.A., Ochoa-Landín, L., Chesley, J.T., Zurcher, L., 2005. Laramide porphyry Cu-Mo mineralization in northern Mexico: Age constraints from Re-Os geochronology in molybdenite. Econ. Geol. 100, 1605–1616.

Byrne, K., Trumbull, R.B., Lesage, G., Gleeson, S.A., Ryan, J., Kyser, K., Lee, R.G., 2020. Mineralogical and Isotopic Characteristics of Sodic-Calcic Alteration in the Highland Valley Copper District, British Columbia, Canada: Implications for Fluid Sources in Porphyry Cu Systems. Econ. Geol. 115, 841–870.

Cao, K., Xu, J.-F., Chen, J.-L., Huang, X.-X., Ren, J.-B., Zhao, X.-D., Liu, Z.-X., 2016. Double-layer structure of the crust beneath the Zhongdian arc, SW China: U-Pb geochronology and Hf isotope evidence. J. Asian Earth Sci. 115, 455–467.

Carpentier, M., Weis, D., Chauvel, C., 2013. Large U loss during weathering of upper continental crust: The sedimentary record. Chem. Geol. 340, 91–104.

Cooke, D.R., 2005. Giant Porphyry Deposits: Characteristics, Distribution, and Tectonic Controls. Econ. Geol. 100, 801–818.

Debon, F., Le Fort, P., 1983. A chemical–mineralogical classification of common plutonic rocks and associations. Earth Env. Sci. T. R. Soc. 73, 135–149.

Deng, J., Wang, Q., Li, G., Li, C., Wang, C., 2014. Tethys tectonic evolution and its bearing on the distribution of important mineral deposits in the Sanjiang region. SW China. Gondwana Res. 26, 419–437.

Dong, T., Du, B., Duan, Z.Y., Cao, X.M., Song, X.F., Dong, H.G., Zhang, Y.M., Li, B., 2022. Metallogenic regularity and prospecting direction of tungsten deposits in Shangri-La area, NW Yunnan Province, China. Sedimentary Geology and Tethyan Geology 42, 62–74 in Chinese with English abstract.

Fan, W.M., Zhang, C.H., Wang, Y.J., Guo, F., Peng, T.P., 2008. Geochronology and geochemistry of Permian basalts in western Guangxi Province, Southwest China: Evidence for plume-lithosphere interaction. Lithos 102, 218–236.

Förster, H.-J., Tischendorf, G., Trumbull, R., Gottesmann, B., 1999. Late-collisional granites in the Variscan Erzgebirge. Germany. J. Petrol. 40, 1613–1645.

Franz, L., Romer, R.L., de Capitani, C., 2013. Protoliths and phase petrology of whiteschists. Contrib. Mineral. Petrol. 166, 255–274.

Gao, X., Yang, L.-Q., Meng, J.-Y., Zhang, L.-J., 2017. Zircon U-Pb, molybdenite Re–Os geochronology and Sr–Nd–Pb–Hf–O–S isotopic constraints on the genesis of Relin Cu–Mo deposit in Zhongdian, Northwest Yunnan. China. Ore Geol. Rev. 91, 945–962.

Gao, X., Yang, L.-Q., Orovan, E.A., 2018. The lithospheric architecture of two subterranes in the eastern Yidun Terrane, East Tethys: Insights from Hf–Nd isotopic mapping. Gondwana Res. 62, 127–143.

Grant, J.A., 2005. Isocon analysis: A brief review of the method and applications. Phys. Chem. Earth, Parts A/B/C 30, 997–1004.

Gresens, R.L., 1967. Composition-volume relationships of metasomatism. Chem. Geol. 2, 47–65.

Heinrich, C.A., 1990. The chemistry of hydrothermal tin (-tungsten) ore deposition. Econ. Geol. 85, 457–481.

Hou, Z.Q., Ma, H.W., Zaw, K., Zhang, Y.Q., Wang, M.J., Wang, Z., Pan, G.T., Tang, R.L., 2003. The Himalayan Yulong porphyry copper belt : Product of large-scale strike-slip faulting in eastern Tibet. Econ. Geol. 98, 125–145.

Hou, Z.Q., Gao, Y.F., Qu, X.M., Rui, Z.Y., Mo, X.X., 2004. Origin of adakitic intrusives generated during mid-Miocene east–west extension in southern Tibet. Earth Planet. Sc. Lett. 220, 139–155.

Hou, Z.Q., Zaw, K., Pan, G.T., Mo, X.X., Xu, Q., Hu, Y.Z., Li, X.Z., 2007. Sanjiang Tethyan metallogenesis in S.W. China: Tectonic setting, metallogenic epochs and deposit types. Ore Geol. Rev. Ore Geology Reviews 31, 48–87.

Hou, Z.Q., Yang, Z.M., Lu, Y.J., Kemp, A., Zheng, Y.C., Li, Q.Y., Tang, J.X., Yang, Z.S., Duan, L.F., 2015. A genetic linkage between subduction- and collision-related porphyry Cu deposits in continental collision zones. Geology 43, 247–250.

Hou, Z.Q., Wang, R., Zhang, H.J., Zheng, Y.C., Jin, S., Thybo, H., Weinberg, R.F., Xu, B., Yang, Z.M., Hao, A.W., Gao, L., Zhang, L.T., 2023. Formation of giant copper deposits in Tibet driven by tearing of the subducted Indian plate. Earth-Sci. Rev. 243, 104482.

Huang, M.-L., Bi, X.-W., Hu, R.-Z., Gao, J.-F., Xu, L.-L., Zhu, J.-J., Shang, L.-B., 2019. Geochemistry, in-situ Sr-Nd-Hf-O isotopes, and mineralogical constraints on origin and magmatic-hydrothermal evolution of the Yulong porphyry Cu Mo deposit. Eastern Tibet. Gondwana Res. 76, 98–114.

Jackson Jr., W.T., Robinson, D.M., Weislogel, A.L., Jian, X., 2020. Cenozoic reactivation along the Late Triassic Ganzi-Litang suture, eastern Tibetan Plateau. Geosci. Front. 11, 1069–1080.

Lei, X.F., Romer, R.L., Glodny, J., Jiang, S.Y., 2023. Geochemical significance of lithium and boron isotopic heterogeneity evolving during the crystallization of granitic melts. Geology 51, 581–585.

Li, W.-C., Pan, G.-T., Zhang, X.-F., Wang, L.-Q., Zhou, J.-X., 2021. Tectonic evolution and multi–episodic metallogenesis of the Sanjiang Paleo-Tethys multi-arc-basin-terrane system, SW Tibetan Plateau. J. Asian Earth Sci. 221, 104932.

Li, W.C., Yin, G.H., Yu, H.J., Lu, Y.X., Liu, X.L., 2011. The porphyry metallogenesis of Geza volcanic magmatic arc in NW Yunnan. Acta Petrol. Sin. 27, 2541–2552 (in Chinese with English abstract).

Li, W.C., Yu, H.J., Gao, X., Liu, X.L., Wang, J.H., 2017. Review of Mesozoic multiple magmatism and porphyry Cu–Mo (W) mineralization in the Yidun Arc, eastern Tibet Plateau. Ore Geol. Rev. 90, 795–812.

Li, W.C., Zhang, X.F., Yu, H.J., Tao, D., Liu, X.L., 2022. Geology and mineralization of the Pulang superlarge porphyry copper deposit (5.11 Mt) in Shangri-la, Yunnan Province, China: A review. China Geol. 5, 662–695.

Liew, T., Hofmann, A., 1988. Precambrian crustal components, plutonic associations, plate environment of the Hercynian Fold Belt of central Europe: indications from a Nd and Sr isotopic study. Contrib. Mineral. Petrol. 98, 129–138.

Liu, X.L., Li, W.C., Zhang, N., Yang, F.C., 2016. Geochemistry and petrogenesis of Triassic mineralized porphyries in the Geza of the Sanjiang orogenic belt, southwestern China. Int. Geol. Rev. 59, 965–980.

López-Moro, F.J., 2012. EASYGRESGRANT—A Microsoft Excel spreadsheet to quantify volume changes and to perform mass-balance modeling in metasomatic systems. Comput. Geosci. 39, 191–196.

Lowell, J.D., 1970. Lateral and vertical alteration-mineralization zoning in porphyry ore deposits. Econ. Geol. 65, 373–408.

Magna, T., Janoušek, V., Kohút, M., Oberli, F., Wiechert, U., 2010. Fingerprinting sources of orogenic plutonic rocks from Variscan belt with lithium isotopes and possible link to subduction-related origin of some A-type granites. Chem. Geol. 274, 94–107.

Magna, T., Novák, M., Cempírek, J., Janoušek, V., Ullmann, C.V., Wiechert, U., 2016. Crystallographic control on lithium isotope fractionation in Archean to Cenozoic lithium-cesium-tantalum pegmatites. Geology 44, 655–658.

Marschall, H.R., Wanless, V.D., Shimizu, N., Pogge von Strandmann, P.A.E., Elliott, T., Monteleone, B.D., 2017. The boron and lithium isotopic composition of mid-ocean ridge basalts and the mantle. Geochim. Cosmochim. Acta 207, 102–138.

Meng, J.Y., 2014. The porphyry Copper-polymetallic deposit in Zhongdian, West Yunan: Magmatism and mineralization. China University of Geosciences, Beijing, pp. 1–189. PhD thesis.(in Chinese with English abstract.

Metcalfe, I., 2021. Multiple Tethyan ocean basins and orogenic belts in Asia. Gondwana Res. 100, 87–130.

Middlemost, E.A.K., 1994. Naming materials in the magma/igneous rock system. Earth Sci. Rev. 37, 215–224.

Moyen, J.-F., Janoušek, V., Laurent, O., Bachmann, O., Jacob, J.-B., Farina, F., Fiannacca, P., Villaros, A., 2021. Crustal melting vs. fractionation of basaltic magmas: Part 1, granites and paradigms. Lithos 402-403.

Pacey, A., Wilkinson, J.J., Boyce, A.J., Millar, I.L., 2020. Magmatic Fluids Implicated in the Formation of Propylitic Alteration: Oxygen, Hydrogen, and Strontium Isotope Constraints from the Northparkes Porphyry Cu-Au District, New South Wales, Australia. Econ. Geol. 115, 729–748.

Peccerillo, A., Taylor, S.R., 1976. Geochemistry of Eocene calc-alkaline volcanic rocks from the Kastamonu area, Northern Turkey. Contrib. Mineral. Petrol. 58, 63–81.

Phelps, P.R., Lee, C.-T.-A., 2022. Extreme lithium isotope fractionation in quartz from the Stewart pegmatite. Geochim. Cosmochim. Acta 336, 208–218.

Proffett, J.M., 2003. Geology of the Bajo de la Alumbrera Porphyry Copper-Gold Deposit, Argentina. Econ. Geol. 98, 1535–1574.

Qi, C.S., Deng, X.G., Li, W.X., Li, X.H., Yang, Y.H., Xie, L.W., 2007. Origin of the Darongshan-Shiwandashan S-type granitoid belt from southeastern Guangxi: geochemical and Sr-Nd-Hf isotopic constraints. Acta Petrol. Sin. 23, 403–412 (in Chinese with English abstract).

Qiu, L., Rudnick, R.L., McDonough, W.F., Merriman, R.J., 2009. Li and δ7Li in mudrocks from the British Caledonides: Metamorphism and source influences. Geochim. Cosmochim. Acta 73, 7325–7340.

Reid, A.J., Wilson, C.J.L., Liu, S., 2005. Structural evidence for the Permo-Triassic tectonic evolution of the Yidun Arc, eastern Tibetan Plateau. J. Struct. Geol. 27, 119–137.

Reid, A., Wilson, C.J.L., Shun, L., Pearson, N., Belousova, E., 2007. Mesozoic plutons of the Yidun Arc, SW China: U/Pb geochronology and Hf isotopic signature. Ore Geol. Rev. 31, 88–106.

Richards, J.P., 2003. Tectono-magmatic precursors for porphyry Cu-(Mo-Au) deposit formation. Econ. Geol. 98, 1515–1533.

Richards, J.P., 2011. Magmatic to hydrothermal metal fluxes in convergent and collided margins. Ore Geol. Rev. 40, 1–26.

Richards, J.P., 2015. Tectonic, magmatic, and metallogenic evolution of the Tethyan orogen: From subduction to collision. Ore Geol. Rev. 70, 323–345.

Romer, R.L., Hahne, K., 2010. Life of the Rheic Ocean: Scrolling through the shale record. Gondwana Gondwana Res. 17, 236–253.

Romer, R.L., Meixner, A., 2014. Lithium and boron isotopic fractionation in sedimentary rocks during metamorphism – The role of rock composition and protolith mineralogy. Geochim. Cosmochim. Acta 128, 158–177.

Romer, R.L., Meixner, A., Förster, H.-J., 2014a. Lithium and boron in late-orogenic granites – Isotopic fingerprints for the source of crustal melts? Geochim. Cosmochim. Acta 131, 98–114.

Romer, R.L., Meixner, A., Hahne, K., 2014b. Lithium and boron isotopic composition of sedimentary rocks — The role of source history and depositional environment: A 250Ma record from the Cadomian orogeny to the Variscan orogeny. Gondwana Res. 26, 1093–1110.

Romer, R.L., Förster, H.-J., Glodny, J., 2022. Role of fractional crystallization, fluid-melt separation, and alteration on the Li and B isotopic composition of a highly evolved composite granite pluton: The case of the Eibenstock granite, Erzgebirge, Germany. Lithos 422–423, 106722.

Rudnick, R., Gao, S., 2003. Composition of the continental crust. In: Rudnick, R.L. (Ed.), The Crust. Treatise on Geochemistry. Elsevier-Pergamon, Oxford, 1–64 (Chap. 63.

Schatz, O.J., Dolejš, D., Stix, J., Williams-Jones, A.E., Layne, G.D., 2004. Partitioning of boron among melt, brine and vapor in the system haplogranite–H2O–NaCl at 800 C and 100 MPa. Chem. Geol. 210, 135–147.

Schmidt, C., Romer, R.L., Wohlgemuth-Ueberwasser, C.C., Appelt, O., 2020. Partitioning of Sn and W between granitic melt and aqueous fluid. Ore Geol. Rev. 117, 103263.

Seedorff, E., Dilles, J.H., Proffett, J.M., Einaudi, M.T., Zurcher, L., Stavast, W.J.A., Johnson, D.A., Barton, M.D., 2005. Porphyry deposits: Characteristics and origin of hypogene features. Soc. Econ. Geol., Inc., Econ. Geol. 100th Anni. Vol, 251–298.
Slack, J.F., Palmer, M.R., Stevens, B.P.J., 1989. Boron isotope evidence for the involvement of non-marine evaporites in the origin of the Broken Hill ore deposits. Nature 342, 913–916.
Stern, C.R., Skewes, M.A., Arévalo, A., 2011. Magmatic Evolution of the Giant El Teniente Cu–Mo Deposit, Central Chile. J. Petrol. 52, 1591–1617.
Teng, F.Z., McDonough, W.F., Rudnick, R.L., Dalpé, C., Tomascak, P.B., Chappell, B.W., Gao, S., 2004. Lithium isotopic composition and concentration of the upper continental crust. Geochim. Cosmochim. Acta 68, 4167–4178.
Tian, Z.-D., Leng, C.-B., Zhang, X.-C., 2020. Provenance and tectonic setting of the Neoproterozoic meta-sedimentary rocks at southeastern Tibetan Plateau: Implications for the tectonic affinity of Yidun terrane. Precambr. Res. 344, 105736.
Tian, H.-C., Tian, S.-H., Hou, Z.-Q., Yang, Z.-M., Zheng, Y., 2022. Lithium isotope fractionation during magmatic differentiation and hydrothermal processes in post-collisional adakitic rocks. Geochim. Cosmochim. Acta 332, 19–32.
Tomascak, P.B., 2004. Developments in the understanding and application of lithium isotopes in the earth and planetary sciences. Rev. Mineral. Geochem. 55, 153–195.
Tomascak, P.B., Langmuir, C.H., le Roux, P.J., Shirey, S.B., 2008. Lithium isotopes in global mid-ocean ridge basalts. Geochim. Cosmochim. Acta. 72, 1626–1637.
Trumbull, R.B., Beurlen, H., Wiedenbeck, M., Soares, D.R., 2013. The diversity of B-isotope variations in tourmaline from rare-element pegmatites in the Borborema Province of Brazil. Chem. Geol. 352, 47–62.
Ulrich, T., 2002. Geology and Alteration Geochemistry of the Porphyry Cu-Au Deposit at Bajo de la Alumbrera. Argentina. Econ. Geol. 97, 1865–1888.
Wang, X.-S., Bi, X.-W., Leng, C.-B., Zhong, H., Tang, H.-F., Chen, Y.-W., Yin, G.-H., Huang, D.-Z., Zhou, M.-F., 2014a. Geochronology and geochemistry of Late Cretaceous igneous intrusions and Mo–Cu–(W) mineralization in the southern Yidun Arc, SW China: Implications for metallogenesis and geodynamic setting. Ore Geol. Rev. 61, 73–95.
Wang, X.-S., Hu, R.-Z., Bi, X.-W., Leng, C.-B., Pan, L.-C., Zhu, J.-J., Chen, Y.-W., 2014b. Petrogenesis of Late Cretaceous I-type granites in the southern Yidun Terrane: New constraints on the Late Mesozoic tectonic evolution of the eastern Tibetan Plateau. Lithos 208–209, 202–219.
Wang, X.-S., Bi, X.-W., Chen, Y.-W., Pan, L.-C., Xu, L.-L., 2019. Crystal fractionation of contaminated melts and re-melting of newly underplated basaltic crust generated Late Triassic andesitic and dioritic intrusions in the southern Yidun Terrane, SW China. Lithos 342–343, 135–151.
Wang, D.-Z., Hu, R., Hollings, P., Bi, X.-W., Zhong, H., Pan, L.-C., Leng, C.-B., Huang, M.-L., Zhu, J.-J., 2021. Remelting of a Neoproterozoic arc root: origin of the Pulang and Songnuo porphyry Cu deposits, Southwest China. Miner. Deposita 56, 1043–1070.
Wang, R., Zhu, D., Wang, Q., Hou, Z., Yang, Z., Zhao, Z., Mo, X., 2020. Porphyry mineralization in the Tethyan orogen. Sci. China Earth Sci. 63, 2042–2067.
Warren, I., Simmons, S.F., Mauk, J.L., 2007. Whole-Rock Geochemical Techniques for Evaluating Hydrothermal Alteration, Mass Changes, and Compositional Gradients Associated with Epithermal Au-Ag Mineralization. Econ. Geol. 102, 923–948.
Wunder, B., Meixner, A., Romer, R.L., Feenstra, A., Schettler, G., Heinrich, W., 2007. Lithium isotope fractionation between Li-bearing staurolite, Li-mica and aqueous fluids: An experimental study. Chem. Geol. 238, 277–290.
Xiang, L., Romer, R.L., Glodny, J., Trumbull, R.B., Wang, R., 2020. Li and B isotopic fractionation at the magmatic-hydrothermal transition of highly evolved granites. Lithos 376–377, 105753.
Xu, B., Hou, Z.Q., Griffin, W.L., Zheng, Y.C., Wang, T., Guo, Z., Hou, J., Santosh, M., O'Reilly, S.Y., 2021a. Cenozoic lithospheric architecture and metallogenesis in Southeastern Tibet. Earth-Sci. Rev 214, 103472.
Xu, R., Romer, R.L., Glodny, J., 2021b. External fluids cause alteration and metal redistribution in the granite-hosted Tangziwa Sn Cu deposit, Gejiu district. China. Lithos 382–383, 105937.
Yan, D.-P., Zhou, Y., Qiu, L., Wells, M.L., Mu, H., Xu, C.-G., 2018. The Longmenshan Tectonic Complex and adjacent tectonic units in the eastern margin of the Tibetan Plateau: A review. J. Asian Earth Sci. 164, 33–57.
Yang, Z.M., Cooke, D.R., 2019. Porphyry Cu Deposits in China. Soc. Econ. Geol. Spec. Publ. 22, 133–187.
Yang, Z.M., Hou, Z.Q., White, N.C., Chang, Z.S., Li, Z.Q., Song, Y.C., 2009. Geology of the post-collisional porphyry copper–molybdenum deposit at Qulong. Tibet. Ore Geol. Rev. 36, 133–159.
Yang, F.C., Li, W.C., Jiang, X.J., Li, C., Wang, Z.Q., Sun, H.Y., Zhou, J.-X., 2020. Late Cretaceous granitic intrusions and associated deposits in the Yidun Arc of the eastern Tibetan Plateau. J. Asian Earth Sci. 192, 104249.
Yin, A., Harrison, T.M., 2000. Geologic evolution of the Himalayan-Tibetan orogen. Annu. Rev. Earth Planet. Sci. 28, 211–280.
Yu, H.-J., Jiang, J.-W., Li, W.-C., 2020. Controls of variable crustal thicknesses on Late Triassic mineralization in the Yidun Arc. Eastern Tibet. J. Asian Earth Sci. 195, 104285.
Zartman, R.E., Doe, B.R., 1981. Plumbotectonics—the model. Tectonophysics 75, 135–162.
Zentilli, M., Maksaev, V., Boric, R., Wilson, J., 2018. Spatial coincidence and similar geochemistry of Late Triassic and Eocene-Oligocene magmatism in the Andes of northern Chile: evidence from the MMH porphyry type Cu–Mo deposit. Chuquicamata District. Int. J. Earth Sci. 107, 1097–1126.
Zhang, X.F., 2018. Magmatism and Mineralization of Compound Massif in Xiuwacu Tungsten-Molybdenum Deposit, Northwest Yunnan Province. China University of Geosciences, Beijing, p. 153. Doctoral dissertation.(in Chinese with English abstract.
Zhang, X.-F., Li, W.-C., Yang, Z., Wang, Y.-Q., 2021. Stable isotope and fluid inclusion constraints on the source and evolution of ore fluids in the Xiuwacu W-Mo granite-related quartz-vein deposit, Yunnan Province. China. Ore Geol. Rev. 136, 104245.